Materials Today Bio 32 (2025) 101665

Contents lists available at ScienceDirect

Materials Today Bio

journal homepage: www.journals.elsevier.com/materials-today-bio

Nanoparticle-mediated sodium butyrate delivery for repairing hypoxic-ischemic brain injury in premature infants

Jing Zhao *, Jun Zhang, Li Hou, Can Yang, Lin Jiang, Daoxin Liang

Department of Neonatology, Affiliated Hospital of North Sichuan Medical College, Nanchong, 637000, China

ARTICLE INFO

Keywords:
Sodium butyrate
Magnetic fluorescent nanoparticles
Sp1
TGF-β1 signaling pathway
Neuronal apoptosis

ABSTRACT

Hypoxic-ischemic encephalopathy of prematurity (HIEP) is a leading cause of acute mortality and chronic neurological injury in premature infants. This study investigates the molecular mechanisms by which magnetic fluorescent nanoparticles loaded with sodium butyrate (MNs@SB) repair HIEP by modulating the Sp1 and TGF-β1 signaling pathways. Untargeted metabolomics analysis revealed significant suppression of the butyrate metabolism pathway in the intestinal tissues of HIEP mice. We synthesized and characterized MNs@SB nanoparticles, with zeta potential and DLS results indicating an average nanoparticle size of approximately 79.89 nm and a zeta potential of −36.87 mV. TEM images confirmed that the nanoparticles formed polymer-coated clusters. MNs@SB demonstrated excellent biocompatibility and stable magnetic targeting behavior. The nanoparticles were delivered to the brain via tail vein injection and magnetic targeting, with focused ultrasound facilitating their diffusion. The results showed that HIEP mice exhibited a significant increase in infarct size and extensive tissue loss, whereas MNs@SB treatment effectively reversed HIEP-induced brain damage, improving both short-term and long-term neurological deficits. Single-cell RNA sequencing and high-throughput transcriptome analysis revealed that MNs@SB promoted brain repair by upregulating neuronal Sp1, activating the TGF-β1 signaling pathway, and inhibiting neuronal apoptosis. In vivo experiments further confirmed that MNs@SB treatment restored SP1 mRNA and protein expression in the brain. Additionally, MNs@SB treatment significantly restored TGF-β1, p-SMAD2, and p-SMAD3 protein expression, indicating activation of the TGF-β1/SMAD2/3 signaling pathway. This study presents a novel nanomedicine therapeutic strategy with potential clinical applications.

1. Introduction

Hypoxic-ischemic encephalopathy of prematurity (HIEP) is one of the most common and severe perinatal brain injuries, playing a critical role in acute mortality and chronic neurological damage in newborns [1–3]. HIEP typically occurs during childbirth due to oxygen deprivation or insufficient blood supply, leading to brain tissue damage and manifesting as various neurological dysfunctions [4–6]. Affected infants may experience cognitive deficits, motor impairments, seizures, and other symptoms, significantly impacting their long-term health and quality of life [7,8]. Currently, treatment options for HIEP include hypothermia therapy, anticonvulsant medications, and supportive care, but these methods have limited efficacy and potential side effects [9]. While hypothermia therapy has been proven to reduce brain injury, its applicability is limited, and the therapeutic window is short [5,10]. Anticonvulsant drugs can help control symptoms but do not effectively prevent the progression of brain damage [3,11]. Supportive care can alleviate some symptoms but cannot fundamentally repair the damaged neural tissue [12–14]. Therefore, there is an urgent need in clinical and research fields to find a new, safe, and effective therapeutic strategy [15].

In recent years, the concept of the gut-brain axis has gained widespread acceptance with the advancement of gut microbiota research [16–18]. The gut-brain axis refers to the complex network through which gut microbes and their metabolites influence central nervous system functions via neural, immune, and endocrine pathways [16,19,20]. Gut microbiota significantly affects the host's physiological and pathological states by metabolizing substances such as short-chain fatty acids (SCFAs) [21–23]. Butyrate, a crucial SCFA, plays a key role in maintaining gut barrier function and influences brain health by

* Corresponding author. Department of Neonatology, Affiliated Hospital of North Sichuan Medical College, No. 63, Wenhua Road, Shunqing District, Nanchong, 637000, Sichuan Province, China.
E-mail address: zhaojingcby@126.com (J. Zhao).

https://doi.org/10.1016/j.mtbio.2025.101665
Received 17 November 2024; Received in revised form 10 March 2025; Accepted 13 March 2025
Available online 14 March 2025

modulating immune responses and inflammation [24–26]. Studies have shown that butyrate can promote brain injury repair by inhibiting neuronal apoptosis and reducing inflammation [27,28]. Additionally, butyrate has demonstrated neuroprotective effects in various neurological diseases, such as Alzheimer's and Parkinson's [29–31]. Therefore, butyrate represents a promising new strategy for the treatment of HIEP, offering significant research and application potential [32–34].

Magnetic nanoparticles (MNs) have garnered significant attention in the field of drug delivery due to their unique advantages [35,36]. MNs combine magnetic targeting and fluorescent imaging capabilities, enabling efficient targeted drug delivery and real-time imaging monitoring [37]. During drug delivery, MNs are guided by an external magnetic field, allowing precise localization to the lesion site and enhancing the therapeutic efficacy of the drug [35,36]. In this study, we synthesized magnetic fluorescent nanoparticles loaded with sodium butyrate (MNs@SB) and validated their excellent magnetic targeting capabilities and biocompatibility through a series of *in vitro* and *in vivo* experiments. MNs@SB were administered via tail vein injection, guided to the brain using an external magnetic field, and further facilitated in crossing the blood-brain barrier (BBB) with focusing ultrasound (FUS) technology, thereby enhancing the distribution efficiency of SB within the brain.

Transcription factor Sp1 and the TGF-β1 signaling pathway play crucial roles in the development, repair, and protection of the nervous system [38–40]. Sp1 is a key transcription factor involved in regulating the expression of numerous genes related to cell proliferation, differentiation, and apoptosis [41–43]. Studies have shown that upregulation of Sp1 expression in the nervous system can promote neuronal survival and functional recovery [44–46]. Similarly, the TGF-β1 signaling pathway plays a significant role in neuroprotection and repair by regulating neuronal survival, apoptosis, and functional recovery [47–49]. In this study, single-cell RNA sequencing (scRNA-seq) and high-throughput transcriptome analysis identified Sp1 as a key gene regulated by MNs@SB in the neurorepair of HIEP. The TGF-β1 signaling pathway was also found to be important in this process.

HIEP through the regulation of Sp1 and TGF-β1 signaling pathways. A series of *in vitro* and *in vivo* experiments were conducted to validate the efficacy and safety of MNs@SB. The results demonstrated that MNs@SB efficiently targeted and delivered SB to damaged brain areas, upregulating neuronal Sp1 expression, activating the TGF-β1 signaling pathway, and inhibiting neuronal apoptosis. This significantly promoted the repair of brain injury in HIEP mice, improving both short-term and long-term neurological deficits. The role of Sp1 was further confirmed through lentivirus-mediated neuronal silencing or overexpression experiments. The novelty of this study lies in the combination of MNs with SB, providing a new therapeutic strategy for the neurorepair of HIEP. This approach offers new research insights and clinical application prospects, demonstrating significant scientific value and potential clinical relevance.

2. Materials and methods

2.1. Ethical statement

This study strictly adhered to the relevant ethical guidelines and regulations for animal experiments. All experimental procedures were approved by the Institutional Animal Care and Use Committee (IACUC). All animals were housed and cared for in a humane environment and were subjected to experiments designed to minimize suffering. At the end of the experiments, all mice were humanely euthanized under ether anesthesia.

2.2. Establishment of the neonatal mouse HIEP model

8-12-week-old SPF-grade C57BL/6J mice (n = 219, purchased from Beijing Vital River Laboratory Animal Technology Co., Ltd., Beijing, China), weighing 20–30 g, were used in this study. All mice were housed individually in SPF-grade animal laboratories under controlled conditions: a 12-h light/dark cycle, humidity of 60 %–65 %, and temperature of 22–25 °C. They had free access to food and water and were acclimated for one week before the start of the experiments. The health status of the mice was monitored before the experiments. The experimental procedures and animal protocols were approved by the Institutional Animal Ethics Committee.

One to three 8-12-week-old female mice were housed with a proven fertile male mouse. Every day between 08:00 and 10:00, vaginal plugs were checked as evidence of mating. The morning a vaginal plug was detected was designated as day 1 of pregnancy. The pregnant female mice were then separated from the male and housed individually under standardized conditions for delivery.

On the 17th day of pregnancy (at 1100 h), pregnant mice were intraperitoneally injected with 200 μL of PBS solution containing 0.5 μg of lipopolysaccharide (LPS, 437650, Sigma-Aldrich, UK) derived from *Salmonella typhimurium* to induce preterm birth. The mice were monitored for signs of delivery every 12 h. Mice that were delivered before the 20th day of pregnancy were classified as preterm and used for subsequent studies. The sample size was determined based on power analysis ($\alpha = 0.05$, power = 0.8) and modeling success rate to detect a 30 % difference in infarct volume between groups. In accordance with the 3R principle, all experimental treatment, control, and sham groups were equally allocated, with n = 6 mice per group. The concentration of MNs@SB was selected based on preliminary pharmacokinetic studies, which indicated that a 200 μL dose (containing 2.5 mg sodium butyrate) achieved the optimal brain accumulation and therapeutic effect. The solubility of MNs@SB in saline was tested to ensure uniform suspension without precipitation.

On postnatal day 7, the neonatal mice were anesthetized with isoflurane in an O_2 mixture (4 % for induction, 2 % for maintenance, at 1 L/min, R510-22-10, RWD, Shenzhen, China). After making an incision in the left side of the neck, the left common carotid artery was isolated. The artery was then doubly ligated with a 6.0 suture and cut between the ligatures. The neck skin was sutured, and lidocaine was applied locally to the wound for analgesia. The entire surgical procedure was completed within 5 min. The pups were then returned to their dam for 1 h before being placed in a hypoxic chamber (8 % O_2 + 92 % N_2, humidified) for 90 min to induce hypoxic injury. During the process, oxygen concentration and incubator temperature were recorded every 5 min to ensure the stability of the hypoxic chamber environment. Upon completion of the hypoxic injury, the mice were immediately returned to their dam. Littermate mice that underwent anesthesia and carotid artery exposure without ligation served as controls (sham). Ischemia-reperfusion (I/R) injury was confirmed using TTC staining, where increased infarct volume and tissue loss in the ipsilateral hemisphere indicated successful model establishment. Inclusion criteria were validated via histological analysis and MRI imaging (not shown). Mice exhibiting abnormal motor function or >20 % weight loss within 24 h post-surgery were excluded. Blood glucose and blood gas levels were monitored pre- and post-surgery using a blood gas analyzer (RAPIDPoint 500, Siemens). Blood pressure measurements were performed using the tail-cuff method, where a sensor cuff was placed on the tail, and blood flow signals were monitored during inflation and deflation. Pre- and post-surgical blood pressure values are presented in Table S1. The experimental procedures and animal usage protocols were approved by the Institutional Animal Ethics Committee [50–52].

2.3. Brain water content test

One week after model establishment or upon completion of drug treatment, the brain tissue of the mice was collected and divided into five parts: ipsilateral basal ganglia (Ipsi-BG), ipsilateral cortex (Ipsi-CX), contralateral basal ganglia (Cont-BG), contralateral cerebral cortex (Cont-CX), and cerebellum. The weight of these five brain regions was

measured before and after drying. Brain regions, including the cortex, hippocampus, and striatum, were analyzed. Peri-infarct regions were identified using MAP2 immunostaining and neuronal viability assays. Tissue samples were collected via perfusion and fixation, followed by microsectioning [53].

2.4. TTC staining

The mouse brain tissue was collected and sliced into 2 mm coronal sections, which were then immersed in 2 % TTC staining solution (G3005, Solarbio, Beijing, China) at 37 °C for 15 min. Red areas indicate normal brain tissue, while white areas indicate infarcted brain tissue. The slices were photographed and analyzed using Image-Pro Plus 6.0 (Media Cybernetics, Bethesda, MD, USA). The percentage of infarct volume for each slice was calculated as follows: (infarct volume/total volume) × 100 %. Infarct volume was determined by integrating infarct areas from consecutive brain slices and quantified using ImageJ software. To correct for ipsilateral swelling, volume adjustments were performed by subtracting the uninjured ipsilateral hemisphere volume from the contralateral hemisphere.

2.5. Nissl staining

Mouse brain tissue was collected and cut into 2 mm coronal sections. The sections were fixed in 4 % paraformaldehyde (PFA, P0099, Beyotime, Shanghai, China) for 20 min and then stained with Nissl staining solution (C0117, Beyotime, Shanghai, China) at 37 °C for 10 min, followed by two washes with distilled water. The sections were then photographed and measured using Image-Pro Plus 6.0 software. Infarct area was defined as the loss of Nissl staining and calculated using the formula: (contralateral area − ipsilateral area/contralateral area) × 100 %

2.6. Immunohistochemistry staining

Paraffin was cooled on ice or at 4 °C and then sectioned. The paraffin sections were placed to dry overnight, and the slides were baked in a 60 °C oven for 20 min. The sections were immersed in xylene (534056, Sigma-Aldrich, USA) for 10 min, followed by a change of xylene and another 10-min immersion. After rehydrating in anhydrous ethanol (1012772, Sigma-Aldrich, USA) for 5 min, the sections were rehydrated again in fresh anhydrous ethanol for 5 min. Subsequently, they were rehydrated in 95 % ethanol and 70 % ethanol for 10 min each, followed by a 5-min rinse in distilled water. The sections were immersed in citrate buffer (pH 6.0, C2488, Sigma-Aldrich, USA) and heated in a microwave on high power for 8 min, then allowed to cool to room temperature. The sections were washed with PBS (pH 7.2–7.6, phosphate-buffered saline, P5493, Sigma-Aldrich, USA) three times for 3 min each. Next, 3 % H_2O_2 (88597, Sigma-Aldrich, USA) was added to the sections, and they were incubated at room temperature for 10 min to inactivate endogenous peroxidases. The sections were then washed three times with PBS for 3 min each. Finally, a normal goat serum-blocking solution (E510009, Sangon Biotech, Shanghai, China) was added, and the sections were incubated at room temperature for 20 min.

After blocking, the sections were incubated with rabbit anti-MAP2 primary antibody (PA5-85755, dilution 1:100, Thermo Fisher, USA) at 4 °C overnight. The next day, the sections were washed three times with PBS. Then, goat anti-rabbit IgG secondary antibody (ab6721, dilution 1:5000, Abcam, Cambridge, UK) was added, and the sections were incubated for 30 min. Following this, the Streptavidin-Biotin Complex (SABC, P0603, Beyotime, Shanghai, China) was added, and the sections were incubated at 37 °C for 30 min in a constant temperature box. Using a DAB staining kit (P0203, Beyotime, Shanghai, China), one drop of each chromogenic reagent was added to the specimen, and the color was allowed to develop for 6 min. The sections were then counterstained with hematoxylin for 30 s. The sections were dehydrated in 70 %, 80 %, 90 %, and 95 % ethanol and anhydrous ethanol for 2 min each, followed by two 5-min immersions in xylene for clearing. The sections were mounted with neutral resin and observed under an upright microscope (BX63, Olympus, Japan). For each section, five random high-power fields were selected for observation. Images were analyzed for average optical density using Image-Pro Plus 6.0 software. Each experiment was repeated three times.

2.7. Assessment of brain injury

Brain injury was evaluated based on infarct volume, total hemispheric tissue loss, and neuropathological scoring.

Total hemispheric tissue damage was quantified using MAP2 immunohistochemical staining to assess the volume of tissue loss and pathological scoring of different brain regions. The entire evaluation process was performed in a single-blind manner (i.e., the evaluator was unaware of the sample grouping). Microimage (Olympus) was used to measure MAP2-positive and MAP2-negative areas in each layer of the sections. According to the Cavalieri principle, the overall tissue damage volume was calculated using the following formula based on the MAP2-positive area: $V = \Sigma A \cdot P \cdot T$, where V is the total volume, ΣA is the sum of the measured areas, P is the reciprocal of the sampling fraction, and T is the section thickness. The total hemispheric tissue damage volume was calculated by subtracting the stained area of the ipsilateral hemisphere from the stained area of the contralateral hemisphere.

For neuropathological assessment, a semiquantitative neuropathological scoring system was used to evaluate brain injury in different regions after HIEP. Sections were stained with MAP2 and scored by an observer blinded to the animals' genotypes and groupings. The cortical injury was scored on a scale of 0–4, where 0 indicated no apparent injury, and 4 indicated extensive confluent infarction involving the majority of the cerebral cortex. The hippocampus, striatum, and thalamus were assessed based on developmental impairment (atrophy) with possible scores of 0–3 and grossly visible cell injury/infarction with possible scores of 0–3. Each brain region received a neuropathological score ranging from 0 to 6. The total score for each animal was obtained by summing the scores from the four different brain regions, resulting in a total possible score ranging from 0 to 22.

2.8. Transmission electron microscopy (TEM)

Mouse brain tissue samples were prepared for observation using TEM. Brain tissue samples were fixed in 2.5 % glutaraldehyde (P1126, Solarbio, Beijing, China) solution at 4 °C for 2 h. After washing three times with PBS, the samples were fixed in 1 % osmium tetroxide (115355, AiKe Reagents, Chengdu, China) solution for 2 h. The samples were then dehydrated at room temperature through a graded ethanol series (50 %, 70 %, 80 %, 90 %, and 95 %), followed by pure acetone (AX0125, Sigma-Aldrich, USA). The samples were treated with a pure embedding agent (4583, Sakura, USA) overnight. The infiltrated samples were embedded and heated at 70 °C overnight to obtain embedded specimens. The embedded samples were sectioned using a Reichert ultramicrotome to obtain 70–90 nm ultrathin sections. These sections were stained with lead citrate solution (HD17810, Hede Biotechnology, Beijing, China) and saturated uranyl acetate solution (CD106833, Howeipharm, Guangzhou, China) in 50 % ethanol, each for 15 min. The stained sections were then observed and imaged using a Hitachi H-7500 transmission electron microscope (Hitachi, Japan).

2.9. Untargeted metabolomics sequencing analysis

For untargeted metabolomics analysis, intestinal tissue samples were collected from sham-operated mice (sham group, n = 6) and HIEP mice (HIEP group, n = 6) one week after model establishment. Approximately 60 mg of intestinal tissue was weighed and placed into a 1.5 mL centrifuge tube containing 40 μL of internal standard (methanol solution

containing 0.3 mg/mL L-2-chlorophenylalanine, 103616-89-3, Shanghai kanglang Biotechnology co., Ltd., Shanghai, China) for gas chromatography-mass spectrometry (GC/MS) preprocessing. The samples were thoroughly homogenized using a homogenizer or ultrasonic processor to ensure all cells were lysed and metabolites were released. The homogenates were then centrifuged at 12,000 g for 10 min at 4 °C to remove cell debris and insoluble materials. The supernatant was transferred to a new centrifuge tube. Ice-cold methanol was added to the supernatant, mixed thoroughly, and the mixture was left to stand at −20 °C for 1 h. After standing, the mixture was centrifuged again to precipitate proteins and other macromolecules. The supernatant was carefully transferred to a new centrifuge tube. The solvent in the supernatant was completely evaporated using a vacuum concentrator or freeze dryer to obtain the dried metabolite extracts.

The dried metabolite extracts were dissolved in 50 % methanol (1.06035, Sigma-Aldrich, USA) in preparation for MS analysis. The dissolved samples were filtered through a 0.22 μm filter to remove any particulate matter. Then, 300 μL of each sample was transferred to a 1.5 mL polypropylene tube and mixed with 900 μL of 80 % methanol containing 0.1 % formic acid (1.59013, Sigma-Aldrich, USA). The mixture was vortexed for 2 min and then centrifuged at 12,000 g for 10 min. The supernatant was transferred to autosampler vials. The samples were analyzed using an Agilent 7890B GC system coupled with an Agilent 5977A MSD system (Agilent Technologies, USA). The injector temperature was maintained at 260 °C. The injection volume in splitless mode was 1 μL. The collision energy was set to 70 eV. MS data were acquired in full scan mode with a mass range of m/z 50–500.

Unsupervised principal component analysis (PCA) was performed using the prcomp statistical function in R. The results were visualized with the "ggplot2" package. The distance matrix between samples was calculated using the verdict function, followed by Principal Coordinates Analysis (PCoA) using the phone function. The results of the PCoA analysis were also visualized using the "ggplot2" package. The obtained data were preprocessed to prevent overfitting using orthogonal Partial Least Squares Discriminant Analysis (PLS-DA) and permutation tests (100 permutations) with the "MixOmics" package. In the PLS-DA model, metabolites with a VIP score >1 and p-value <0.05 were identified as differential metabolites (DMs). Additionally, univariate analysis was combined with this approach to select metabolites with a fold change ≥ 2 or ≤ 0.5 and a p-value <0.05 in Student's t-test as the final DMs. MetaboAnalyst (Version 5.0) was used to identify the related metabolic pathways.

2.10. Preparation of MNs loaded with SCFAs

Synthesis of Iron Oxide Nanoparticles (Fe_3O_4 NPs): Mix 2 mmol Fe (acac)3 (517003, Sigma-Aldrich, USA), 10 mmol 1,2-hexadecanediol (213748, Sigma-Aldrich, USA), 6 mmol oleic acid (OX0165, Sigma-Aldrich, USA), 6 mmol oleylamine (909831, Sigma-Aldrich, USA), and 20 mL benzyl ether (108014, Sigma-Aldrich, USA). Stir the mixture under a nitrogen atmosphere. After stirring the mixture for 30 min, transfer it to a stainless steel autoclave lined with polytetrafluoroethylene (PTFE). Heat the mixture to 200 °C and maintain this temperature for 2 h. Then, under a nitrogen atmosphere, increase the temperature to 300 °C and hold it for 1 h. After heating, allow the mixture to cool to room temperature while stirring. The resulting Fe_3O_4 NPs are then washed several times with deionized water and ethanol through centrifugation to obtain the final Fe_3O_4 NPs.

Synthesis of MNs: Disperse 200 μL of Fe_3O_4 NPs in n-hexane (PHR1555, Sigma-Aldrich, USA) and wash the dispersion three times with ethanol to remove impurities. Dissolve the NPs in tetrahydrofuran (1601770, Sigma-Aldrich, USA) and add dopamine hydrochloride (DOPA, 1225204, Sigma-Aldrich, USA) under ultrasonic conditions. Stir the mixture for 2 h under non-magnetic conditions, then centrifuge at 14,800 rpm to collect the precipitate. Dissolve the precipitate in ddH_2O under ultrasonic conditions, then centrifuge again at 14,800 rpm to remove excess DOPA. The resulting product is a Fe_3O_4-DOPA aqueous dispersion.

Add 25 % polyacrylic acid (PAA, 435325, Sigma-Aldrich, USA) to the Fe_3O_4-DOPA aqueous dispersion in a 1:1 ratio and stir under non-magnetic conditions for 6 h to obtain Fe_3O_4-DOPA-PAA. Dissolve the product in ddH_2O and centrifuge at 14,800 rpm three times. Then, add mPEG2k-NH_2 (Q-0261515, Xi'an Kylom Biotechnology, Xi'an, China) and stir under non-magnetic conditions overnight. Centrifuge at 3,000 rpm to remove large particles, then centrifuge again at 14,800 rpm to remove excess mPEG2k-NH_2. Resuspend the precipitate to obtain a brown, transparent aqueous dispersion of Fe_3O_4-DOPA-PAA-PEG, which are the MNs.

For loading SB, dissolve SB (2.5 mg, 567430, Sigma-Aldrich, USA), Cy5.5-PEG2K-NH2 (20 mg, R-22150-2K, Xi'an Ruixi Biological Technology Co., Ltd., Xi'an, China), EDC (2 mg, 1-(3-dimethylaminopropyl)-3-ethylcarbodiimide, 39391, Sigma-Aldrich, USA), and NHS (2 mg, N-hydroxysuccinimide, 8.04518, Sigma-Aldrich, USA) in dimethyl sulfoxide (DMSO, D2650, Sigma-Aldrich, USA). Stir the mixture at 37 °C overnight. Dialyze the mixture using a 3000 KD dialysis bag to remove DMSO and any remaining small molecules, collecting the Cy5.5-SB aqueous solution. Mix the Cy5.5-SB aqueous solution with the Fe_3O_4-DOPA-PAA-PEG aqueous dispersion. Stir the mixture under non-magnetic conditions overnight. Centrifuge the mixture at 14,800 rpm to collect the final product. Dissolve the final product in 0.9 % NS (sodium chloride injection, Harbin Medisan Pharmaceutical CO.,LTD., Harbin, China) to obtain MNs@SB for experimental use. Use a UV–Vis–NIR spectrophotometer (PerkinElmer Lambda 750) to record the absorbance at a wavelength of 200 nm (with a mass extinction coefficient of 0.22 L mg^{-1} cm^{-1}) to quantify the loading capacity of SB. Characterize the NPs using an FEI Tecnai F20 transmission electron microscope and a PANalytical X-ray diffractometer (Empyrean). The magnetic properties of the nanoclusters are characterized at 300 K using a Physical Property Measurement System (Quantum Model 6000, USA).

2.11. Morphology, size, and distribution of NPs

The size and shape of the NPs were observed using TEM. To prepare for scanning, load 20 μL of freshly prepared NP sample onto a carbon-coated copper electron microscope grid. Stain the sample with 1 % uranyl acetate (CD106833, Howeipharm, Guangzhou, China) for 5 min to provide high-quality contrast and clarity. Wash the grid three times with PBS and use filter paper to remove excess phosphotungstic acid solution, maintaining the grid in a semi-dry state. The images were observed using a Hitachi H7650 transmission electron microscope (Hitachi, Japan) at 100 KV.

Nanoparticle Tracking Analysis (NTA): Dissolve 20 μg of NPs in 1 mL of PBS, vortex for 1 min to ensure uniform distribution of the NPs. Use the ZetaView NP tracking analyzer (Particle Metrix, Germany) to directly observe and measure the particle size distribution of the NPs. Measure the average particle size and polymer dispersity index (PDI) of the exosomes using dynamic light scattering (DLS) and determine the Zeta potential of the exosomes. Perform three measurements for each sample.

2.12. Drug concentration detection

For drug concentration detection, first perform spectral scans of Cy5.5 and SB separately using a UV–Vis spectrophotometer. Prepare and measure a series of solutions with known concentrations to establish their respective standard curves. Next, dilute the Cy5.5-SB composite drug samples and measure their absorbance. Use the standard curves to calculate the actual concentrations of Cy5.5 and SB in the samples, as well as their relative proportions. For MNs@SB samples, determine the concentration of Cy5.5 by measuring its absorbance and then calculate the effective SB concentration based on the ratio of Cy5.5 to SB. To comprehensively evaluate the active ingredients and metal content in

the drug complex, ICP-OES was used to detect the iron concentration in the samples. Briefly prepare a series of iron standard solutions to accurately calibrate the ICP-OES equipment and establish a calibration curve. Once the instrument is calibrated, introduce the prepared sample solutions into the high-temperature plasma through a nebulizer, where iron atoms are excited and emit characteristic spectra. The instrument accurately detects these spectra, and the iron content in the samples is quantitatively analyzed based on the emission intensity. Process the collected data using the instrument software, comparing the emission spectra with the calibration curve to calculate the actual iron concentration. Perform repeated measurements to ensure the accuracy of the results.

2.13. Isolation and identification of mouse neurons

Collect the brain tissue from euthanized mice and place it in a sterile D-Hanks solution (PB180321, Wuhan Pricella Biotechnology Co., Ltd., Wuhan, China) in a petri dish. Wash off the surface blood of the brain and transfer it to another petri dish containing fresh D-Hanks solution. Using tweezers, carefully lift the cerebral cortex along the mid-sagittal plane on the dorsal surface to expose the "C"-shaped hippocampus in the mid-sagittal plane. Carefully separate the entire dentate gyrus of the hippocampus using tweezers. Under a dissecting microscope, remove any other tissues and choroid plexus covering the dentate gyrus. Cut the dentate gyrus tissue into small pieces and transfer them to a vial. Allow the tissue fragments to settle, then remove the supernatant D-Hanks solution. Digest the tissue with 0.25 % trypsin (25200056, Gibco, USA) and pipette up and down 14–20 times to create a cell suspension. Filter the suspension through a mesh sieve. Take a small amount of the cell suspension, mix it with an equal amount of trypan blue, and add it to a hemocytometer for cell density counting under a 100× inverted microscope. Seed the cells in a 24-well culture plate at a density of 2×10^5 cells/mL. Culture the cells in Neurobasal Medium (21103-049, Thermo Fisher, USA) supplemented with 2 % B27 (17504-044, Thermo Fisher, USA), 100 U/mL penicillin-streptomycin (15140-122, Thermo Fisher, USA), and 2 mM L-glutamine (25030081, Thermo Fisher, USA). Incubate the cells at 37 °C in a 5 % CO_2 incubator, and replace the medium every 3 days.

Neurons were identified by staining with a neurospecific enolase (NSE) antibody (PA5-78384, 1:100, Thermo Fisher, USA). The cells were fixed with 4 % PEA and permeabilized with 0.2 % Triton X-100 (P0096, Beyotime, Shanghai, China) for 5 min. The sections were then blocked with 10 % normal goat serum. Next, the rabbit anti-NSE antibody was added, and the cells were incubated overnight at 4 °C. After washing with PBS, an Alexa Fluor 488-conjugated goat anti-rabbit IgG secondary antibody (ab150077, 1:300, Abcam, UK) was applied and incubated at room temperature for 1 h. Following another PBS wash, the slides were mounted and observed under a fluorescence microscope (BX63, Olympus, Japan). A positive immunofluorescence rate greater than 90 % indicated successful isolation of neurons.

Induction of Neuronal Hypoxia and Ischemia (H/I): The oxygen deprivation experiment was conducted in a specially designed hypoxic chamber (InVivO2 400, Ruskinn Technologies) at a temperature of 37 °C with 5 % CO_2. The internal oxygen sensor continuously monitored the oxygen concentration. Cells were exposed to 1 % O_2 for up to 48 h. Ischemia was simulated *in vitro* using the oxygen-glucose deprivation (OGD) method. Neurons were exposed to OGD conditions with a glucose-free medium (11966025, Gibco) under hypoxic and near-anoxic conditions. The cells were divided into three groups: the control group, where neurons were subjected to ischemia and hypoxia induction without treatment; the MNs@SB + sh-NC group, where neurons were subjected to ischemia and hypoxia induction and treated with MNs@SB; and the MNs@SB + sh-Sp1 group, where neurons with silenced Sp1 were subjected to ischemia and hypoxia induction and treated with MNs@SB.

2.14. In vitro biosafety evaluation

BV2 mouse microglia (CL-0493, Wuhan Pricella Biotechnology Co., Ltd., Wuhan, China) were purchased for the study. BV2 microglia were cultured in DMEM/F12 medium (PM150315, Wuhan Pricella Biotechnology Co., Ltd., Wuhan, China) supplemented with 10 % FBS (10100147C, Thermo Fisher, USA) and 1 % penicillin-streptomycin (100 U/mL penicillin and 100 μg/mL streptomycin, 15140163, Thermo Fisher, USA). To assess the cytotoxicity of the nanopreparations, different doses of MNs (MNs@SB) were added to the culture medium of neurons and microglia and incubated for 12 and 24 h. Cell viability was determined using the Cell Counting Kit-8 (CCK-8) assay. Briefly, CCK-8 was added to the cell cultures and incubated for 2 h. The absorbance of the solution at 450 nm was measured using a microplate reader to quantify cell viability. The absorbance levels directly reflected the number of viable cells.

All cells were cultured in a humidified incubator at 37 °C with 5 % CO_2 (Heracell™ Vios 160i CR CO_2 Incubator, 51033770, Thermo Scientific™, Germany).

2.15. Hemolysis assay detection

To conduct the hemolysis assay for MNs@SB, prepare solutions of MNs@SB at various concentrations ranging from 100 μg/mL to 3.13 μg/mL. Set PBS as the negative control and deionized water as the positive control. Fresh human whole blood with an anticoagulant (EDTA) was obtained from IPHASE (Suzhou) Co., Ltd., Suzhou, China. The blood was mixed with each concentration of MNs@SB solutions and control liquids at a specific ratio, then incubated at 37 °C for 3 h. After incubation, the samples were centrifuged at 2000 g for 10 min to separate the undissolved cellular components (CC) from the plasma. The supernatant was collected, and the absorbance was measured at 540 nm using a spectrophotometer to quantify the amount of hemoglobin released into the blood, indicating the level of hemolysis.

2.16. In vivo and in vitro magnetic targeting evaluation

For the *in vitro* magnetic targeting evaluation, first set up a magnetic field with a surface magnetic field strength of 3000 Gauss. Place a petri dish containing MNs@SB in the magnetic field and observe the adsorption behavior of MNs@SB under the influence of the magnetic field. Pay special attention to whether any NPs escape the designated circular area. Use both natural light and fluorescence imaging to demonstrate the aggregation effect of MNs@SB in the magnetic field.

In vivo Magnetic Targeting Evaluation: HIEP mice were randomly divided into four groups: Cy5.5-SB group, MNs@SB group, MNs@SB + Magnetic Attraction group, and MNs@SB + Magnetic Attraction + FUS group. After HIEP induction, Cy5.5-SB and MNs@SB were administered to different groups of mice (3 mice per group) via tail vein injection. In the MNs@SB + Magnetic Attraction group and MNs@SB + Magnetic Attraction + FUS group, a magnet was fixed to the head of the mice 1 h after tail vein injection. Additionally, in the MNs@SB + Magnetic Attraction + FUS group, FUS at approximately 500 kHz was applied to the head for 10 min. Two hours post-injection, *in vivo* imaging was performed using the IVIS Lumina Series (PerkinElmer, USA) to observe the magnetic targeting of the NPs. Previous studies have demonstrated that ultrasound at 1 MHz effectively facilitates nanoparticle entry into the brain [54–57]. Therefore, 500 kHz FUS was selected in this study to validate its efficacy in enhancing BBB permeability.

2.17. In vitro and in vivo release experiments

The *in vitro* release efficiency of MNs@SB was evaluated by measuring sodium butyrate release at different time points. A dialysis bag containing 3 mL of MNs@SB (34.4 μg/mL) was immersed in 30 mL of PBS (pH 7.4) at 37 °C under 30 rpm orbital shaking (Tecnal TE-420,

São Paulo, Brazil). At predetermined time points (6, 12, 18, and 24 h), 1 mL of receiver medium was withdrawn and replaced with an equal volume of fresh PBS. Sodium butyrate release from nanoparticles was quantified using a previously validated HPLC method. The release kinetics of NaBu from nanoparticles/CS was analyzed using zero-order, Higuchi, first-order, and Korsmeyer-Peppas mathematical models [58–60].

In vivo release was assessed by collecting plasma samples at 6, 12, 18, and 24 h post-MNs@SB treatment and quantifying sodium butyrate using HPLC. Results indicated sustained release over 24 h [58].

2.18. Experimental animal grouping and treatment

The HIEP model was established in preterm mice as described. The sham operation group consisted of mice with only the right common carotid artery isolated but not ligated and without hypoxia treatment. The treatment groups were divided as follows: Sham group: Sham-operated mice treated with PBS via tail vein injection; PBS group: HIEP model mice treated with PBS via tail vein injection; MNs group: HIEP model mice treated with MNs via tail vein injection; MNs@SB group: HIEP model mice treated with MNs@SB via tail vein injection. Each group consisted of 10 preterm mice, and the HIEP model was established as described. One day after model establishment, treatments were administered via tail vein injection. The mice were anesthetized with isoflurane and received daily tail vein injections of 200 μL of the respective treatments for two weeks. After each injection, a magnet was taped to the head of the mice for 1 h to facilitate magnetic targeting and accumulation. Subsequently, FUS at approximately 500 kHz was applied to the scalp for 10 min to enhance drug diffusion. During the treatment period, 0 to 4 mice per group died. After the treatment course, 6 mice from each group were randomly selected for neurological assessment and then euthanized for further experimental analysis.

2.19. Cytokine detection before and after treatment

Blood samples were collected before and after treatment (1 mL venous blood), centrifuged at 3000 rpm for 10 min at 4 °C, and plasma was stored at −80 °C. ELISA kits were used to measure IL-6 (JL33712, Jianglai Biotech), CRP (JL13637, Jianglai Biotech), and TNF-α (JL10484, Jianglai Biotech). CRP levels were measured using an immunoturbidimetric method with a CRP kit on an Olympus 2700 automated biochemical analyzer. ELISA procedures were conducted according to the manufacturer's instructions. Five different concentrations of standards and serum samples were added to each well of an ELISA plate, incubated at 60 °C for 1 h, and washed using an automatic plate washer (DEM-3). Colorimetric development was performed using substrate solutions and stopped with a termination reagent. Absorbance (OD values) was measured using a Bio-RAD680 microplate reader. Cytokine concentrations were calculated using a standard curve generated from five standard concentrations [61].

2.20. Hematoxylin and eosin (H&E) staining

H&E staining was performed using a H&E staining kit (C0105S, Beyotime, Shanghai, China) to observe the pathological changes in the heart, liver, spleen, and kidney tissues of mice. Tissue samples were fixed in 4 % PFA (P0099, Beyotime, Shanghai, China), dehydrated, cleared, and embedded in paraffin. The paraffin-embedded tissues were sectioned into 5 μm thick slices using a microtome. The sections were then baked, deparaffinized, and rehydrated in water. They were stained with hematoxylin, washed with distilled water, and immersed in 95 % ethanol. Subsequently, the sections were stained with eosin, differentiated in 70 % acid ethanol, dehydrated, cleared, and mounted with neutral balsam. Finally, the morphological changes in the heart, liver, spleen, and kidney tissues were observed under a light microscope.

2.21. TUNEL detection of cell apoptosis

Cell apoptosis in tissue samples was detected using a TUNEL staining kit (C1088, Beyotime, Shanghai, China). Briefly, mouse brain tissue was fixed with 4 % PEA for 30 min and washed three times with PBS. The tissue was then permeabilized with PBS containing 0.3 % Triton X-100 for 3 min, incubated at room temperature for 5 min, and washed twice with PBS. Next, 50 μL of TUNEL detection solution was added, and the tissue was incubated at 37 °C in the dark for 60 min. After washing three times with PBS, the tissue was counterstained with DAPI (10 μg/mL) for 10 min. The sections were mounted with an anti-fluorescence quenching mounting medium and observed under a fluorescence microscope. Cy3 was used with an excitation wavelength of 550 nm and an emission wavelength of 570 nm (red fluorescence). The proportion of apoptotic cells in each group was calculated using Image-Pro Plus 6.0 software.

2.22. Short-term neurological assessment

On days 3, 5, and 7 after model establishment, six mice from each group were randomly selected for behavioral tests to assess short-term neurological function. The two tests included Negative Geotaxis and Front-limb Suspension. Each mouse was tested three times, and the average of the three scores was recorded.

For the Negative Geotaxis test, each mouse was placed on an inclined plane (30 cm in length, inclined at 45°) with its head pointing downward. After holding the mouse in this position for 5 s, it was released, and the time taken for the mouse to turn its head upward within 30 s was recorded. For the Front-limb Suspension test, each mouse's forepaws were placed on a suspended wire, and the time taken for the mouse to fall off the wire within 60 s was recorded.

2.23. Long-term neurological assessment

After completing the treatment, six mice from each group were randomly selected for the following two behavioral tests to evaluate their long-term neurological function.

Novel Object Recognition Test (NORT): Before the experiment, mice were placed in an open field (60 × 40 × 40 cm) for 10 min per day for three consecutive days to acclimate to the testing conditions. At the start of the test, mice were placed in the open field for 10 min. Subsequently, two balls of the same color were placed in the open field, and the time the mice spent interacting with the balls over 20 min was recorded. Interaction was defined as the mice touching the balls with their nose or mouth. Between trials, the apparatus and objects were cleaned with 50 % ethanol to minimize olfactory cues. One hour after the first test, the mice were tested again for 20 min using a new object (with a different shape and color) to replace one of the familiar objects from the first test. The time spent by the mice exploring the new object and the familiar object was recorded. The discrimination ratio was calculated as the time spent on the new object divided by the total time spent on both the new and familiar objects: Discrimination Ratio = Time on New Object/(Time on New Object + Time on Familiar Object).

Morris Water Maze Test (MWMT): The MWMT was conducted in a black cylindrical tank (120 cm in diameter, 60 cm deep). A tracking system was used to record the animals' movements during the test. The water maze was divided into four equal quadrants, with a platform placed below the water surface in the center of the third quadrant. All mice were trained for five consecutive days prior to the experiment to locate the platform. During the test, the mice were placed in different quadrants of the maze, and tracking software was used to record the time it took for each mouse to find the platform. On the sixth day, the platform's position was changed, and the mice were allowed to swim freely in the maze for 60 s. The time taken by the mice to reach the platform was recorded using the SMART video tracking system. The Morris water maze video tracking system comprises both testing instruments and analytical software. This system can measure indices of

memory behavior in animals, with the computer automatically tracking and monitoring their movements. Utilizing a color image processing algorithm, the system tracks the mice's movement trajectories in real time. It analyzes various metrics, including the paths and time spent in the four quadrants, efficiency across six cycles, directional angles, average movement speed; time spent passing the virtual platform, and the duration of stay on the virtual platform.

2.24. Preparation of sequencing samples

The brain tissues obtained from the PBS and MNs@SB groups of mice were washed with ice-cold PBS to remove residual non-brain tissues and to disrupt the tissues. The samples were then digested at 37 °C for 30 min in a solution containing 1 mg/mL collagenase (C2674, Sigma-Aldrich, USA), 1 unit/mL DNase I, and 10 % FBS in DMEM (11965092, Thermo Fisher, USA). The digestion mixture, along with the remaining tissues, was filtered through a 200-mesh sieve. The filtrate was centrifuged at 4 °C for 5 min at 50×*g*. The supernatant was discarded, and the pellet was resuspended in a complete DMEM medium. This washing and resuspension process was repeated twice. Red blood cells were removed using a red blood cell lysis buffer (C3702-120 mL; Beyotime, Shanghai, China). Apoptotic and dead cells were eliminated using the Annexin V Dead Cell Removal Kit (17899, StemCell Technologies, Canada) through immunomagnetic cell separation. The resulting cell pellet was resuspended in PBS to obtain sequencing samples. The activity, integrity, and count of the cells in the prepared sequencing samples were assessed using microscopy and flow cytometry.

2.25. scRNA-seq and data analysis

Brain tissue samples from the PBS group (n = 1) and the MNs@SB treatment group (n = 1) were evaluated and captured using the C1 Single-Cell Auto Prep System (Fluidigm, Inc., South San Francisco, CA, USA). After cell capture, cells were lysed on-chip to release mRNA, which was then reverse-transcribed into cDNA. The cDNA underwent preamplification on a microfluidic chip for subsequent sequencing. The amplified cDNA libraries were constructed and sequenced on the HiSeq 4000 Illumina platform (parameters: paired-end reads, read length 2 × 75 bp, approximately 20,000 reads per cell).

Data analysis was performed using the "Seurat" package in R software. Quality control standards were set to 200 < nFeature_RNA <5000 and percent.mt < 20, and the top 2000 highly variable genes were selected. To reduce the dimensionality of the scRNA-seq dataset, PCA was conducted based on these highly variable genes. The first 20 principal components (PCs) were chosen for downstream analysis using the ElbowPlot function in the "Seurat" package. Major cell subpopulations were identified using the FindClusters function with the resolution parameter set to the default (res = 1). Non-linear dimensionality reduction was then performed on the scRNA-seq data using the t-distributed Stochastic Neighbor Embedding (t-SNE) algorithm. Marker genes for various cell subpopulations were identified using the "Seurat" package, and cell annotation was performed based on lineage-specific marker genes in conjunction with the online CellMarker database. Cell communication analysis was conducted using the "CellChat" package in R. Differentially expressed genes (DEGs) within the scRNA-seq dataset were identified using the "Limma" package in R, with DEGs between different samples selected based on criteria of $|\log2FC| > 1$ and p-value <0.05.

2.26. High-throughput transcriptome sequencing

High-throughput transcriptome sequencing samples were prepared from mouse brain tissues using the described methods. The samples were grouped into the PBS group (n = 3) and the MNs@SB treatment group (n = 3). Following validation of RNA purity and integrity, high-throughput transcriptome sequencing was performed.

RNA Purity and Integrity Validation: RNA purity was assessed using the Nanodrop ND-1000 spectrophotometer (Thermo Fisher) by measuring the OD260/280 ratio to ensure the absence of protein and organic contaminants. RNA concentration was measured using the Qubit RNA Assay Kit (Q33221, Thermo Fisher, USA). Total RNA samples meeting the following criteria were used for subsequent experiments: RNA Integrity Number (RIN) ≥ 7.0 and a 28S:18S rRNA ratio ≥1.5.

Sequencing libraries were generated and sequenced by CapitalBio Technology (Beijing, China). A total of 5 μg RNA was used for each sample. Briefly, ribosomal RNA (rRNA) was removed from the total RNA using the Ribo-Zero Magnetic Kit (MRZG12324, Epicentre, USA). Sequencing libraries were constructed using the NEB Next Ultra RNA Library Prep Kit for Illumina (E7760S, NEB, USA). The RNA was fragmented into approximately 300 base pair (bp) fragments in NEBNext First Strand Synthesis Reaction Buffer (5×). First-strand cDNA was synthesized using reverse transcriptase and random primers, followed by the synthesis of second-strand cDNA in the Second Strand Synthesis Reaction Buffer (10×) containing dUTP Mix. The cDNA fragments underwent end repair, including the addition of poly(A) tails and the ligation of sequencing adapters. Following the ligation of Illumina sequencing adapters, the second strand of cDNA was digested with USER Enzyme (M5508, NEB, USA) to construct a strand-specific library. The DNA library was then amplified, purified, and enriched via PCR. Library quality was assessed using the Agilent 2100 Bioanalyzer, and the library was quantified with the KAPA Library Quantification Kit (KK3605, Merck, USA). Finally, paired-end sequencing was performed on the Illumina NextSeqCN500 sequencer.

2.27. Transcriptome sequencing data analysis

The quality of raw paired-end reads from the sequencing data was checked using FastQC software v0.11.8. Preprocessing of the raw data was performed with Cutadapt software v1.18 to remove Illumina sequencing adapters and poly(A) tails. Reads containing more than 5 % Ns were removed using a Perl script. The FASTX Toolkit v0.0.13 was used to extract reads with at least 70 % of bases having a quality score above 20. BBMap software was employed to repair paired-end sequences. Finally, the filtered high-quality reads were aligned to the mouse reference genome using HISAT2 software v0.7.12.

Differential expression analysis of mRNA read counts was performed using the "Limma" package in R, with the selection criteria set to $|\log2FC| > 1$ and p-value <0.05. Venn analysis to identify intersecting genes was conducted using the "VennDiagram" package in R. For the intersecting genes, Gene Ontology (GO) enrichment analysis was carried out using the "ClusterProfiler" package in R, encompassing biological processes (BP), molecular functions (MF), and CC. The results of the GO enrichment analysis were visualized with bubble plots and chord diagrams. Candidate targets were subjected to the Kyoto Encyclopedia of Genes and Genomes (KEGG) enrichment analysis using the "ClusterProfiler" package in R, with a selection criterion of $|\log2FC| > 1$. The KEGG enrichment results were also visualized with bubble plots and chord diagrams. Additionally, a Friends analysis was performed using the "GOSemSim" package in R.

2.28. Immunofluorescence staining

Fresh cell or tissue samples were fixed in 4 % PEA for 24 h, followed by a graded alcohol dehydration process and xylene clearing. The samples were then embedded in paraffin. Tissue sections, 4–5 μm thick, were cut using a microtome and flattened in a 40 °C water bath before being transferred onto slides. The sections were treated with xylene twice for 5 min each, followed by graded dehydration in 100 %, 95 %, and 70 % alcohol for 5 min each, and rinsed with distilled water. Antigen retrieval was performed by heating the sections in a microwave in citrate buffer (pH 6.0) until boiling for 5 min, then allowing them to cool to room temperature naturally. The sections were washed three times with

PBS for 5 min each, then fixed in ice-cold methanol at −20 °C for 30 min. After removing the methanol, the sections were washed three more times with PBS for 5 min each. The sections were incubated in 0.1 % Triton X-100 (P0096, Beyotime) at room temperature for 15 min, followed by three additional washes with PBS for 5 min each, completing the preparation of the sections.

After blocking with BSA for 30 min, primary antibodies were applied: rabbit anti-NSE (PA5-78384, 1:100, Thermo Fisher, USA) and rabbit anti-SP1 (PA5-115954, 1:100, Thermo Fisher, USA). The sections were incubated at 37 °C for 60 min. Subsequently, the sections were washed three times with PBS for 5 min each. DAPI staining was then performed for 10 min, followed by three PBS washes to remove excess DAPI (C1002, Beyotime, Shanghai, China). After washing, 20 μL of mounting medium was added to cover the sections. Once the mounting medium had dried, the sections were observed and photographed using a fluorescence microscope. Images were analyzed using ImageJ Pro Plus 6.0 software. Quantification was based on the fluorescent coverage area within a fixed field of view at 40 × magnification. The average value from six different fields was calculated, and each experiment was repeated three times.

2.29. Reverse transcription quantitative polymerase chain reaction (RT-qPCR) for gene expression analysis

Total RNA was extracted from tissues and cells using the Trizol Reagent (A33254, Thermo Fisher, USA) and reverse transcribed into cDNA using the Reverse Transcription Kit (RR047A, Takara, Japan). The reaction mixture for RT-qPCR was prepared with the SYBR® Premix Ex Taq™ II Kit (DRR081, Takara, Japan), and the RT-qPCR was performed on an ABI7500 Real-Time PCR System (Thermo Fisher, USA). The PCR program was set as follows: initial denaturation at 95 °C for 30 s, followed by 40 cycles of denaturation at 95 °C for 5 s and annealing at 60 °C for 30 s. This was followed by an extension at 95 °C for 15 s, further extension at 60 °C for 60 s, and a final extension at 90 °C for 15 s to generate the amplification curve. GAPDH was used as the internal control. Each RT-qPCR assay was performed in triplicate wells, and the experiment was repeated three times. The relative expression of target genes in the experimental group compared to the control group was calculated using the $2^{-\Delta\Delta Ct}$ method. The formula is $\Delta\Delta Ct = \Delta Ct_{\text{experimental group}} - \Delta Ct_{\text{control group}}$, where $\Delta Ct = Ct_{\text{target gene}} - Ct_{\text{internal control gene}}$. Ct is the number of cycles needed to reach the threshold of real-time fluorescence intensity, indicating exponential amplification. Primer sequences are listed in Table S2.

2.30. Western blot

Total protein was extracted from tissues and cells using RIPA lysis buffer (P0013B, Beyotime, Shanghai, China) containing 1 % PMSF (Phenylmethanesulfonyl fluoride) following the manufacturer's instructions. The protein concentration of each sample was determined using a BCA Protein Assay Kit (P0011, Beyotime, Shanghai, China) and adjusted to 1 μg/μL. Each sample (100 μL) was boiled at 100 °C for 10 min to denature the proteins and then stored at −80 °C until use. Based on the size of the target protein bands, 8 %–12 % SDS-PAGE (Sodium dodecyl sulfate-polyacrylamide gel electrophoresis) gels were prepared. Protein samples (50 μg) were loaded equally into each lane using a micropipette. The proteins were separated by electrophoresis at a constant voltage, starting at 80 V and then increasing to 120 V for 2 h. The separated proteins were transferred to a PVDF membrane (1620177, Bio-Rad, USA) using a constant current of 250 mA for 90 min.

The PVDF membrane was blocked with 5 % non-fat milk in 1 × TBST at room temperature for 1 h, followed by discarding the blocking solution and washing the membrane with 1 × TBST for 10 min. The membrane was then incubated overnight at 4 °C with the primary antibodies (details in Table S3). After primary antibody incubation, the membrane was washed three times with 1 × TBST for 10 min each. Next, the membrane was incubated at room temperature for 1 h with HRP-conjugated secondary antibodies: either goat anti-rabbit IgG (ab6721, 1:5000, Abcam, Cambridge, UK) or goat anti-mouse IgG (ab205719, 1:5000, Abcam, Cambridge, UK). Following secondary antibody incubation, the membrane was washed three times with 1 × TBST for 5 min each. The membrane was then immersed in ECL reagent (1705062, Bio-Rad, USA) at room temperature for 1 min. Excess reagent was removed, and the membrane was covered with plastic wrap. The protein bands were visualized using the Image Quant LAS 4000C imaging system (GE, USA). GAPDH was used as the internal control for total cellular protein. The relative protein expression levels were quantified by measuring the grayscale ratio of the target protein bands to the GAPDH bands. Each experiment was repeated three times for consistency.

2.31. Lentivirus transfection

Neurons were silenced using lentivirus infection, with lentivirus packaging services provided by Sangon Biotech (Shanghai, China). The plasmids used included the pSuper-retro-puro series and auxiliary plasmids gag/pol and VSVG (catalog numbers #113535, #14887, and #8454, all purchased from Addgene, USA). These plasmids were packaged into lentiviruses by Sangon Biotech. The constructed plasmids were co-transfected into HEK293T cells using Lipofectamine 2000 reagent (11668030, Thermo Fisher, USA). After 48 h of cell culture, the supernatant was collected, filtered through a 0.45 μm filter, and centrifuged to collect the virus. The supernatant was collected again at 72 h, centrifuged, and concentrated. The viral titers were determined by combining the viruses collected at both time points.

When the cells reached the logarithmic growth phase, they were digested with trypsin and seeded into 6-well plates at a density of 1×10^5 cells per well. After 24 h of regular culture, when the cells reached approximately 75 % confluence, the culture medium was replaced with medium containing the packaged lentivirus (MOI = 10, working titer approximately 5×10^6 TU/mL) and 5 μg/mL polybrene (TR-1003, Sigma-Aldrich, UK) for infection. After 4 h of infection, an equal volume of fresh culture medium was added to dilute the polybrene. The medium was then replaced with a fresh culture medium 24 h post-infection. For the construction of a stable cell line, cells were continuously cultured in a medium containing 2 μg/mL puromycin (E607054, Sangon Biotech, Shanghai, China). During passaging, the concentration of puromycin was gradually increased in a stepwise manner to 2, 4, 6, 8, and 10 μg/mL for resistance selection to obtain the stable cell line. Once the cells stopped dying in the puromycin-containing medium, they were collected, and the knockout efficiency was verified using Western blot and RT-qPCR. The sequences for the silencing lentivirus are provided in Table S4, and the sequence with the best silencing effect was chosen for subsequent experiments.

Cell groupings: sh-NC neurons (control cells) and sh-Sp1 neurons (Sp1-silenced cells).

2.32. CCK-8 assay for cell viability

Neurons were digested and resuspended, and the cell concentration was adjusted to 1×10^5 cells/mL. Cells were then seeded into 96-well plates at 100 μL per well and cultured overnight under standard conditions. According to the instructions of the CCK-8 kit (C0041, Beyotime, Shanghai, China), cell viability was assessed at 12, 24, 36, and 48 h post-culture. For each time point, 10 μL of CCK-8 solution was added to each well, and the plates were incubated at 37 °C in a 5 % CO_2 incubator for 2 h. The absorbance at 450 nm was measured using a microplate reader (BioTek, USA). Cell viability was calculated using the following formula:

$$\textit{Cell viability}\ (\%) = \left(\frac{OD_{sample} - OD_{blank}}{OD_{control} - OD_{blank}}\right) \times 100$$

OD_{sample} is the optical density of the drug-treated sample. $OD_{control}$ is

the optical density of the control group (untreated cells under normal growth conditions). OD_{blank} is the optical density of the blank control (containing culture medium and CCK-8 reagent but no cells).

2.33. EdU staining

Neurons were seeded into 24-well plates at a density of 1×10^5 cells per well, with three replicates for each group. EdU (5-Ethynyl-2′-deoxyuridine) solution (ST067, Beyotime, Shanghai, China) was added to the culture medium to a final concentration of 10 μmol/L, and the plates were incubated for 2 h. After incubation, the medium was removed, and the cells were fixed with PBS containing 4 % PEA at room temperature for 15 min. The cells were then washed twice with PBS containing 3 % BSA, followed by incubation with PBS containing 0.5 % Triton-100 at room temperature for 20 min. The cells were washed again twice with PBS containing 3 % BSA. Next, 100 μL of staining solution was added to each well, and the cells were incubated in the dark at room temperature for 30 min. The nuclei were stained with DAPI for 5 min. After mounting the slides, 6–10 random fields of view were observed under a fluorescence microscope (FM-600, Shanghai Pudan Optical Instrument Co., Ltd.). The number of positive cells in each field was recorded. The EdU labeling rate (%) was calculated as follows: EdU Labeling Rate (%) = Number of Positive Cells/(Number of Positive Cells + Number of Negative Cells) × 100 %. Each experiment was repeated three times.

2.34. Flow cytometry for apoptosis detection

Neuronal apoptosis was detected using the Annexin V-FITC/PI Apoptosis Detection Kit (C1062L, Beyotime, Shanghai, China). Cells were seeded into 6-well plates at a density of 1×10^6 cells per well. After incubation, the cells were collected and resuspended in 195 μL of Annexin V-FITC binding buffer. Then, 5 μL of Annexin V-FITC solution and 10 μL of PI solution were added, and the cells were incubated at room temperature in the dark for 15 min. Flow cytometry analysis was performed within 20 min using a BD FACSCalibur flow cytometer to determine the apoptosis rate. The apoptosis rate was calculated as the sum of the apoptotic cell proportions in the Q1-UR (upper right) and Q1-LR (lower right) quadrants.

2.33. Statistical analysis

Data were obtained from at least three independent experiments and are presented as mean ± standard deviation (Mean ± SD). Comparisons between the two groups were performed using an independent samples *t*-test. A one-way analysis of variance (ANOVA) was used to compare three or more groups. If ANOVA indicated significant differences, Tukey's HSD post-hoc test was conducted to compare the differences between groups. For non-normally distributed data or data with unequal variances, the Mann-Whitney *U* test or Kruskal-Wallis H test was used. All statistical analyses were performed using GraphPad Prism 9.5.0 (GraphPad Software, Inc.) and R version 4.2.1 (R Foundation for Statistical Computing). A significance level of 0.05 was set for all tests, with two-sided p-values less than 0.05 considered statistically significant and *p*-values greater than 0.05 considered not significant.

3. Results

3.1. Metabolomics analysis reveals the significant role of butyrate salt metabolism in the development and progression of HIEP

To investigate the role of the "microbiota-gut-brain" axis in the neurorepair mechanisms of HIEP, we surgically constructed a mouse model of HIEP. One week after model construction, the mice were euthanized to obtain their brain tissues. As shown in Fig. S1A, compared to the sham group (control), the HIEP model group exhibited significant brain edema and a marked increase in water content in various brain regions (Fig. S1B). TTC and Nissl staining results indicated that, compared to the sham group, the HIEP model group had a significantly increased infarct area in the brain and extensive tissue loss (Figs. S1C–D).

TEM revealed that neurons in the ipsilateral hemisphere of the sham group exhibited abundant cytoplasm and intact cell membranes. In contrast, neurons in the ipsilateral hemisphere of the model group were severely damaged, with a significant reduction in organelles, swollen mitochondria and endoplasmic reticulum, presence of vacuoles, and unclear or partially absent nuclear membranes (Fig. S1E). We further assessed tissue loss and brain pathology scores using MAP2 immunostaining. The results indicated that compared to the sham group, the model group mice showed a significant increase in striatum and hippocampus volume loss and pathological scores (Figs. S1F–G). These findings confirm the successful construction of the HIEP mouse model.

To further investigate whether HIEP affects intestinal tissue homeostasis in mice, we collected intestinal tissue samples from both the sham and model groups for untargeted metabolomics analysis. The PCA results showed a clear separation between the sham and model groups (Fig. 1A). Similarly, the PLS-DA and PCoA results indicated a distinct separation between the sham and model groups in the score plots (Fig. 1B–C), with permutation analysis showing $R2Y = 0.996 > 0.8$, confirming the stability of the model (Fig. 1D). Differential analysis identified a total of 93 DMs between the sham and model groups, with 20 metabolites upregulated and 73 metabolites downregulated (Fig. 1E, Fig. S2). Next, we conducted a KEGG pathway enrichment analysis on the DMs. The results revealed that these metabolites were significantly enriched in the butyrate metabolism pathway (Fig. 1F–G), with specific pathways and related metabolites detailed in Fig. 1H. We then compared the expression of metabolites related to the butyrate metabolism pathway between the sham and model groups. The findings showed that, compared to the sham group, the model group exhibited increased expression of pyruvate and decreased expression of 4-hydroxybutyrate, L-glutamate, succinate, and (R)-3-hydroxybutyrate (Fig. 1I).

In summary, we successfully constructed a HIEP mouse model. Metabolomics analysis of the intestinal tissue revealed that the butyrate metabolism pathway was significantly inhibited in HIEP mice.

3.2. Successful preparation of MNs loaded with SCFAs

Based on the metabolomics study results, we selected butyrate for subsequent experiments to investigate the role of SCFAs in regulating the "microbiota-gut-brain" axis in the neurorepair mechanisms of HIEP.

MNs@SB consists of modified Fe_3O_4 NPs and Cy5.5-labeled SB. First, Fe_3O_4-DOPA-PAA-PEG (MNs) were modified using a layer-by-layer (LBL) technique, which endowed the MNs with good hydrophilicity and biocompatibility. Subsequently, Cy5.5-labeled SB was loaded onto the MNs through electrostatic adsorption, forming MNs@SB (Fig. 2A). X-ray diffraction (XRD) patterns showed that the main diffraction peaks of the synthesized Fe_3O_4 NPs matched those of Fe_3O_4 (JCPDS No. 19–0629, Fig. 2B). TEM images revealed uniform Fe_3O_4 NPs with a size of 6.82 ± 0.8 nm (Fig. 2C–D). To enhance biocompatibility, DOPA was used to modify the Fe_3O_4 NPs. As a result of successful surface modification, the average particle size of Fe_3O_4-DOPA increased to approximately 15.78 nm, slightly larger than that of Fe_3O_4 NPs (Fig. 2E). Next, PAA and mPEG2k-NH_2 polymers were sequentially coated onto Fe_3O_4-DOPA using the LBL method, resulting in Fe_3O_4-DOPA-PAA-PEG (MNs). The zeta potential and DLS results confirmed the successful surface modification, with the final MNs having an average size of approximately 79.89 nm and a zeta potential of −36.87 mV (Fig. 2F). TEM images of the MNs showed polymer-coated clusters on their surfaces (Fig. 2G).

To better observe drug accumulation in the brain, SB was fluorescently labeled with Cy5.5 using amino acid dehydration condensation, ensuring consistency in fluorescence intensity and drug concentration (Fig. 2A). The UV–visible spectroscopy was employed to

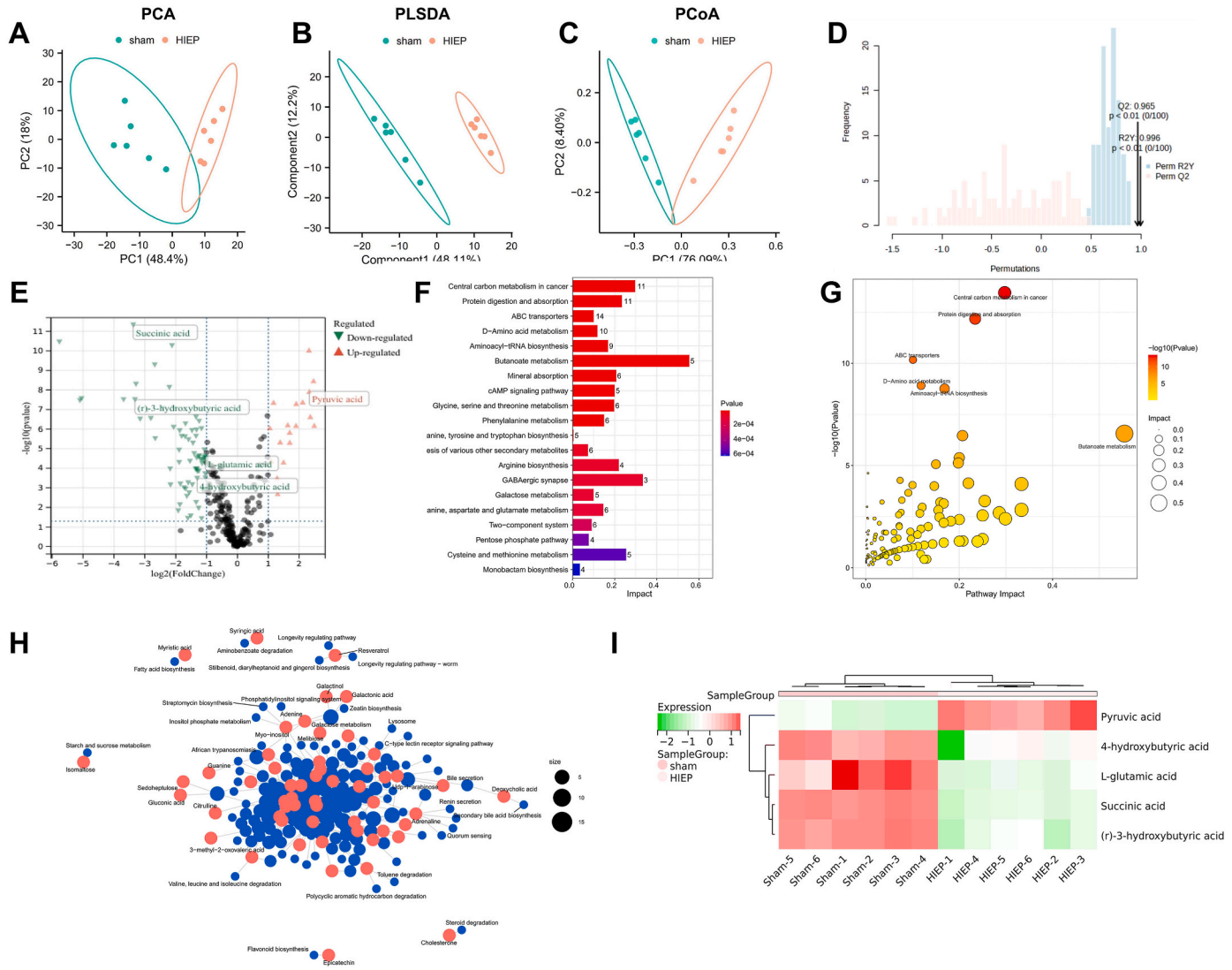

Fig. 1. Untargeted Metabolomics Analysis of Intestinal Tissue in HIEP Mice. Note: (A) PCA score plot of intestinal tissue samples from the sham group (n = 6) and HIEP group (n = 6) mice; (B) PLSDA score plot of intestinal tissue samples from the sham group (n = 6) and HIEP group (n = 6) mice; (C) PCoA score plot of intestinal tissue samples from the sham group (n = 6) and HIEP group (n = 6) mice; (D) Permutation test analysis of intestinal tissue samples from the sham group (n = 6) and HIEP group (n = 6) mice; (E) Volcano plot of DMs in intestinal tissue samples from the sham group (n = 6) and HIEP group (n = 6) mice, where red triangles represent upregulated metabolites, green inverted triangles represent downregulated metabolites, and black dots represent non-DMs; (F) KEGG bar plot of DMs in intestinal tissue samples from the sham group (n = 6) and HIEP group (n = 6) mice, indicating the count of enriched metabolites in each pathway, with colors representing the P-value from hypergeometric distribution tests; (G) KEGG bubble plot of DMs in intestinal tissue samples from the sham group (n = 6) and HIEP group (n = 6) mice; (H) KEGG enrichment analysis of DMs, where blue dots represent enriched pathways, red dots represent metabolites, and larger dots indicate a higher number of associated molecules, with gradient colors representing the log2(FC) value; (I) Heatmap of butyrate salt metabolic pathway-related metabolite expression, with colors ranging from green to red indicating low to high expression levels.

detect the loading capacity of SB in the Cy5.5-SB structure. As shown in Fig. 2H, SB was successfully conjugated with the Cy5.5 fluorescent dye. Detailed characterization of the NPs was performed using TEM and DLS. TEM revealed that the prepared MNs@SB exhibited a typical spherical shape (Fig. 2I). The zeta potential of MNs was approximately −36.87 mV, which changed to −25.68 mV after the electrostatic adsorption of Cy5.5-SB (Fig. 2J). According to DLS results, the average particle size of MNs@SB increased to about 126.47 nm compared to MNs alone (Fig. 2K). Additionally, the UV–visible spectrum of MNs@SB showed characteristic peaks of Cy5.5-SB at approximately 635 nm and 680 nm, indicating the successful loading of Cy5.5-SB onto the MNs (Fig. 2L). Moreover, the hysteresis curve results demonstrated that the final product, MNs@SB, retained magnetic properties comparable to MNs, suggesting that the Cy5.5-SB structure did not significantly affect the magnetism of MNs (Fig. 2M).

Next, we further evaluated the biosafety of MNs@SB. First, *in vitro* CCK-8 assay results indicated that even when the concentration of exogenous iron in the cell culture medium reached approximately 30 $\mu g/mL^{-1}$, the NPs exhibited negligible toxicity to neurons or microglia after 12 and 24 h of exposure (Fig. 3A–B). Additionally, hemolysis assays were conducted to assess the biosafety of MNs@SB in the circulatory system. The results showed that different doses of MNs@SB caused minimal hemolysis of blood cells (Fig. 3C). Additionally, we measured IL-6, TNF-α, and CRP levels in blood samples before and after treatment to evaluate systemic inflammation and confirm the safety of MNs@SB administration. The results demonstrated no significant changes in IL-6, TNF-α, and CRP levels before and after treatment (Fig. 3D). These findings suggest that the synthesized MNs@SB possesses excellent biocompatibility.

Secondly, we verified the fluorescence of MNs@SB using deep red

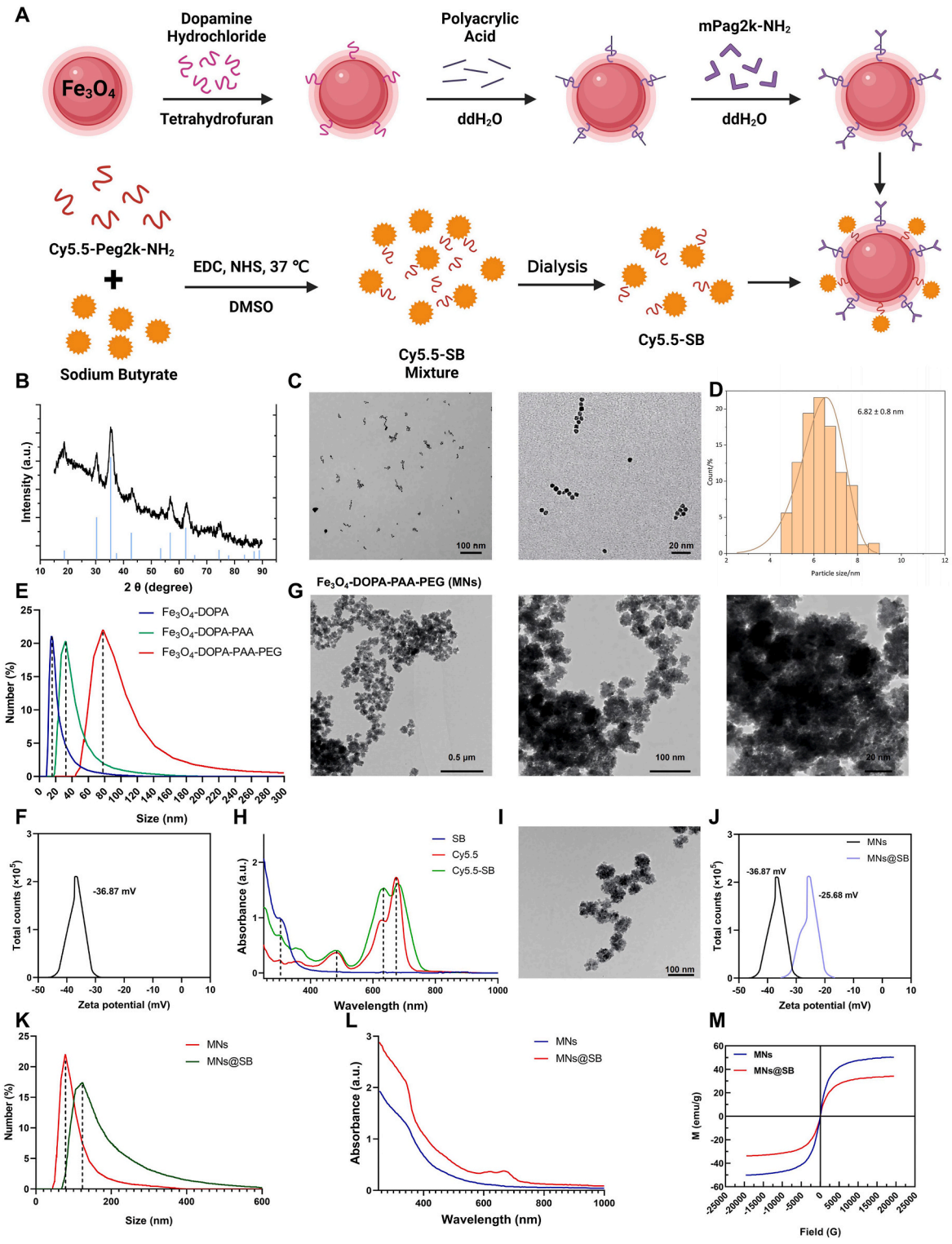

Fig. 2. Synthesis and Characterization of MNs@SB. Note: (A) Schematic diagram of the synthesis process of MNs@SB NPs; (B) XRD spectra of Fe_3O_4 NPs; (C) TEM images showing the morphology of Fe_3O_4 NPs (scale bars: 100 nm/20 nm); (D) NP tracking analysis of the size distribution of Fe_3O_4 NPs; (E) NP tracking analysis of the size distribution of Fe_3O_4-DOPA, Fe_3O_4-DOPA-PAA, and Fe_3O_4-DOPA-PAA-PEG; (F) Zeta potential analysis of MNs; (G) TEM images showing the morphology of MNs (scale bars: 0.5 μm/100 nm/20 nm); (H) UV–Vis absorption spectra of SB, Cy5.5, and Cy5.5-SB; (I) TEM images showing the morphology of MNs@SB (scale bar: 100 nm); (J) Zeta potential analysis of MNs and MNs@SB; (K) NP tracking analysis of the size distribution of MNs and MNs@SB; (L) UV–Vis absorption spectra of MNs and MNs@SB; (M) Hysteresis loops of MNs and MNs@SB. Quantitative data are presented as Mean ± SD, with each experiment repeated three times per group.

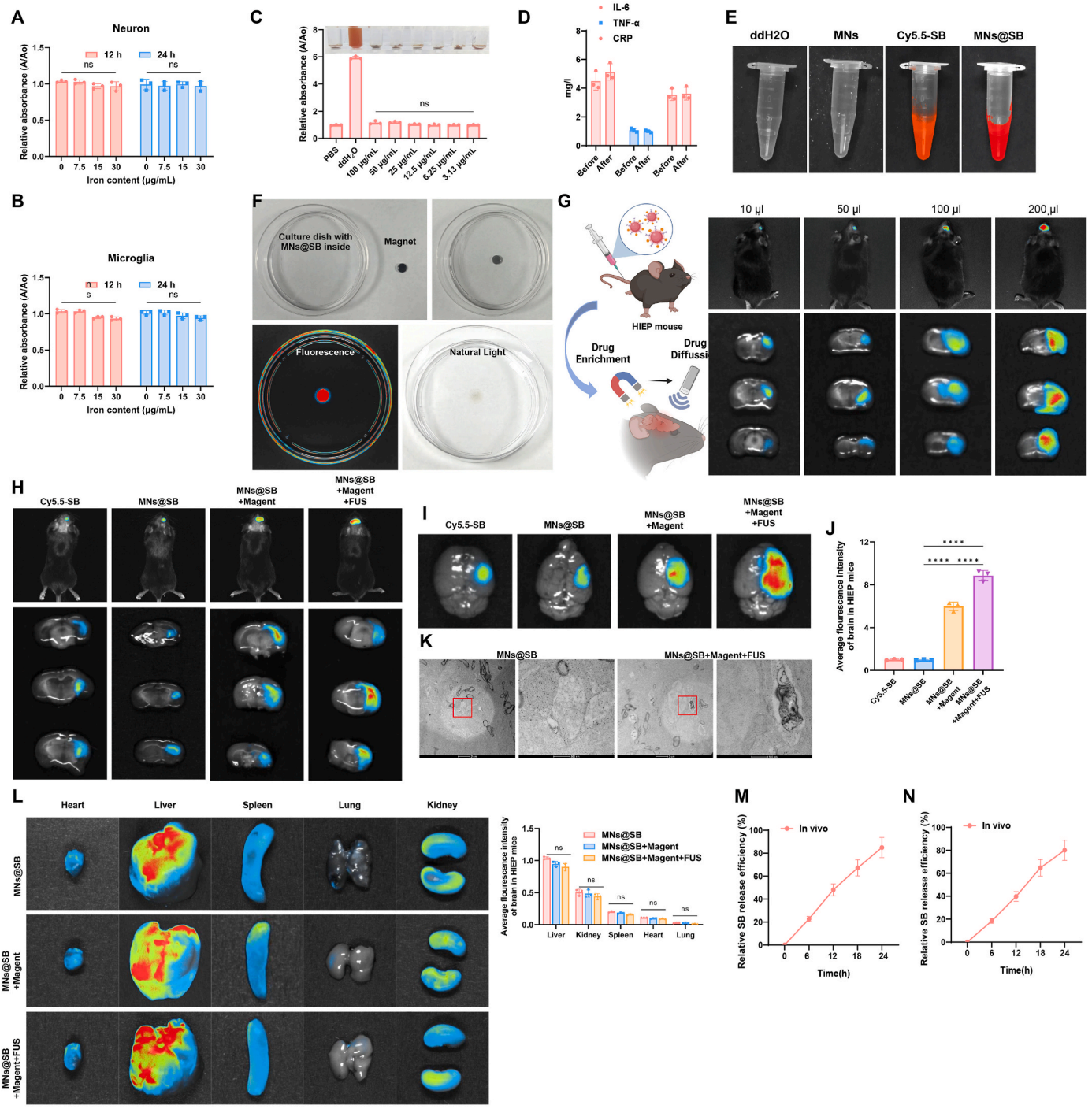

Fig. 3. *In vitro* and *in vivo* Biosafety Evaluation of MNs@SB. Note: (A) Cytotoxicity of MNs@SB on neurons detected by CCK-8 assay, where ns indicates no significant difference compared to the 0 iron ion concentration group; (B) Cytotoxicity of MNs@SB on microglia detected by CCK-8 assay, where ns indicates no significant difference compared to the 0 iron ion concentration group; (C) Hemolysis test results of MNs@SB in the circulatory system, where ns indicates no significant difference compared to the PBS group; (D) IL-6, TNF-α, and CRP levels were measured before and after treatment using ELISA kits; (E) Fluorescence of ddH_2O, MNs, Cy5.5-SB, and MNs@SB under deep red light; (F) Photographs of MNs@SB under natural light and fluorescence images under deep red light in the presence of an external magnetic field; (G) Schematic diagram of the MNs@SB treatment method; (H) Representative fluorescence images of *in vivo* and mouse brain tissue sections 2 hours after administration; (I) Representative images of mouse brain tissue under deep red light; (J) Fluorescence intensity of NPs accumulated in the ipsilateral hemisphere of the brain in different groups of HIEP mice, with $^{****}p < 0.0001$ indicating a significant difference between the two groups; (K) Representative TEM images of mouse brain tissue from different treatment groups; (L) Fluorescence images and average fluorescence intensity of different organs in different groups of mice 2 h after administration, where ns indicates no significant difference between the groups; (M) *In vivo* SB drug release efficiency was assessed at 6 h, 12 h, 18 h, and 24 h; (N) *In vitro* SB drug release efficiency was assessed at 6 h, 12 h, 18 h, and 24 h. Quantitative data are presented as Mean ± SD, with each cell experiment repeated three times and each animal experiment involving three mice per group.

light illumination (Fig. 3E). To confirm the magnetic targeting ability of MNs@SB, we applied an external magnetic field (surface magnetic field strength of 3000 Gauss) to attract all MNs@SB to the magnetic field. The results showed that the NPs were almost entirely retained within the circular magnetic field region, with minimal leakage (Fig. 3F), indicating that MNs@SB exhibits strong and stable magnetic targeting behavior.

We also conducted *in vivo* experiments to test the magnetic targeting and FUS effectiveness of MNs@SB. At a maximum concentration of 100 μg/mL, MNs@SB did not cause hemolysis, and this concentration was selected for subsequent *in vivo* experiments. To further determine the optimal administration volume, different volumes of MNs@SB were intravenously injected. At low doses, fluorescence was barely detectable in the mouse brain, as confirmed by ex vivo brain imaging. However, when 200 μL of MNs@SB was administered, fluorescence in the brain and brain slices significantly increased. Therefore, we established 200 μL at 100 μg/mL as the final *in vivo* experimental concentration (Fig. 3G). As shown in Fig. 3H–J, the heads of mice in the Cy5.5-SB and MNs@SB groups exhibited almost no fluorescence, which was confirmed by ex vivo brain imaging. This indicates that without magnetic attraction or FUS assistance, Cy5.5-SB and MNs@SB could hardly penetrate brain tissue. After applying the magnetic field, the fluorescence in the brains and brain slices of the MNs@SB + Magnet group significantly increased compared to the MNs@SB group, suggesting that magnetic attraction enhances the targeted enrichment of MNs@SB in the brain tissue of the HIEP model. Furthermore, using FUS resulted in more dispersed fluorescence compared to the MNs@SB + Magnet group, confirming that FUS can facilitate a broader distribution of NPs within the brain.

We also captured TEM images showing the intracellular presence of MNs@SB within brain tissue. The administration of MNs@SB using magnetic attraction and FUS significantly increased the accumulation of MNs@SB within cellular organelles (Fig. 3K). To further investigate whether MNs@SB causes damage to major organ tissues, we collected liver, kidney, spleen, heart, and lung tissues from mice in different treatment groups. Fluorescence results showed that 2 h after MNs@SB administration, fluorescence primarily accumulated in the liver and kidneys, indicating that the short-term metabolism of the drug likely depends on liver and kidney function (Fig. 3L). Furthermore, both *in vitro* and *in vivo* release experiments demonstrated that SB release reached approximately 80 % within 24 h (Fig. 3M−N).

Based on the above analysis, we successfully prepared MNs@SB, which demonstrated good biosafety. Additionally, we found that using magnetic attraction and FUS to assist in the delivery of MNs@SB could be a potential therapeutic method for HIEP, as it increases the accumulation of NPs in the brain.

3.3. MN improve brain injury in HIEP mice

To investigate whether synthesized MNs can repair neural damage in HIEP mice through the “microbiota-gut-brain” axis, we constructed a HIEP mouse model and administered treatment via tail vein injection.

First, to assess the impact of NPs on short-term neurological impairment in HIEP mice, we conducted negative geotaxis and forelimb hanging tests on days 3, 5, and 7 after constructing the HIEP model. In the negative geotaxis test (Fig. S3A), compared to the sham group, the time required for the HIEP mice (PBS group) to turn their heads significantly increased. Treatment with MNs alone showed no significant improvement, whereas SB treatment resulted in a slight reduction in time. However, after MNs@SB treatment (MNs@SB group), the time required for the mice to turn their heads decreased significantly (Fig. S3B). In the forelimb hanging test (Fig. S3C), HIEP mice showed reduced hanging time on the wire, Treatment with SB alone slightly increased the hanging time, while MNs@SB treatment significantly increased the hanging time. Treatment with MNs alone did not improve short-term neurological impairment in the mice (Fig. S3D).

To further assess the impact of MNs@SB on long-term neurological impairment in HIEP mice, we conducted NORT and MWMT following treatment completion. NORT results (Fig. S3E) showed that the discrimination index in the PBS and MN-only groups was significantly lower than in the sham group, indicating a severe impairment in distinguishing between novel and familiar objects. This suggests that hypoxic-ischemic injury negatively impacted cognitive function, particularly memory and learning abilities. However, MNs@SB-treated HIEP mice exhibited a significant improvement in memory and learning, whereas SB treatment alone provided slight improvement, and MNs alone had no therapeutic effect (Fig. S3F).

MWMT results (Fig. S3G) demonstrated that PBS-treated mice spent more time searching for the platform and less time in the target quadrant compared to the sham group, indicating severe cognitive impairment. SB treatment alone provided slight improvement, while MNs@SB treatment resulted in significantly better performance than PBS treatment. Notably, swimming speeds remained similar across groups (Fig. S3H), suggesting that prolonged escape latency was primarily due to spatial memory deficits rather than motor impairment (Figs. S3I–J).

After five days of training, the platform was removed, and the mice’s movement trajectories were recorded for 1 min. In the sham group, mice spent approximately 50 % of their time in the target quadrant, whereas PBS-treated mice spent equal time across all quadrants, reflecting a substantial decline in cognitive function and memory. In contrast, MNs@SB treatment significantly improved cognitive performance and memory retention, while SB treatment alone provided moderate improvement, and MNs alone showed no therapeutic effect (Figs. S3K–L). Based on these results, MNs@SB can improve both short-term and long-term neurological deficits caused by HIEP in mice.

We analyzed the survival rates of mice in different treatment groups 14 days post-treatment. The results showed that, compared to the sham group, HIEP significantly reduced survival rates, with a 40 % mortality rate during the treatment period. SB treatment alone increased survival to 80 %, while MNs@SB treatment further improved survival to 90 % (Fig. 4A). Additionally, the results indicated that SB alone had a limited effect on survival, while blank nanoparticles did not significantly improve survival rates. However, compared to the blank nanoparticle group, SB treatment alone still resulted in a significant survival advantage.

After treatment, six mice were randomly selected from each group for brain tissue analysis. Compared to the sham group, HIEP-induced mice exhibited significant brain edema and increased water content in multiple brain regions. Blank nanoparticles had no apparent effect, while SB treatment slightly reduced edema. In contrast, MNs@SB treatment significantly alleviated brain swelling and reduced water content, whereas MNs treatment alone had minimal impact (Fig. 4B–C). TTC and Nissl staining showed that, compared to the sham group, HIEP-induced mice exhibited significantly larger infarct areas and extensive tissue loss. The blank nanoparticle group showed no noticeable improvement, while SB treatment significantly reduced infarct size. Notably, MNs@SB treatment effectively reversed HIEP-induced brain damage, whereas blank nanoparticles and MNs alone did not produce significant neuroprotective effects (Fig. 4D–E).

We also evaluated neuronal apoptosis using TUNEL staining. The results showed that apoptosis levels were significantly increased in the PBS group compared to the sham group. Blank nanoparticles had no apparent effect, while SB treatment alone reduced apoptosis levels. However, MNs@SB treatment effectively reversed apoptosis, demonstrating a strong neuroprotective effect (Fig. 4F). TEM revealed that, compared to the sham group, neurons in the ipsilateral hemisphere of PBS-treated mice exhibited severe damage, including organelle depletion, swollen mitochondria and endoplasmic reticulum, vacuolization, and disrupted nuclear membranes. Blank nanoparticles had no noticeable effect, while SB treatment alone mitigated neuronal damage. MNs@SB treatment further alleviated these morphological abnormalities, preserving cellular integrity (Fig. 4G). MAP2 immunostaining and

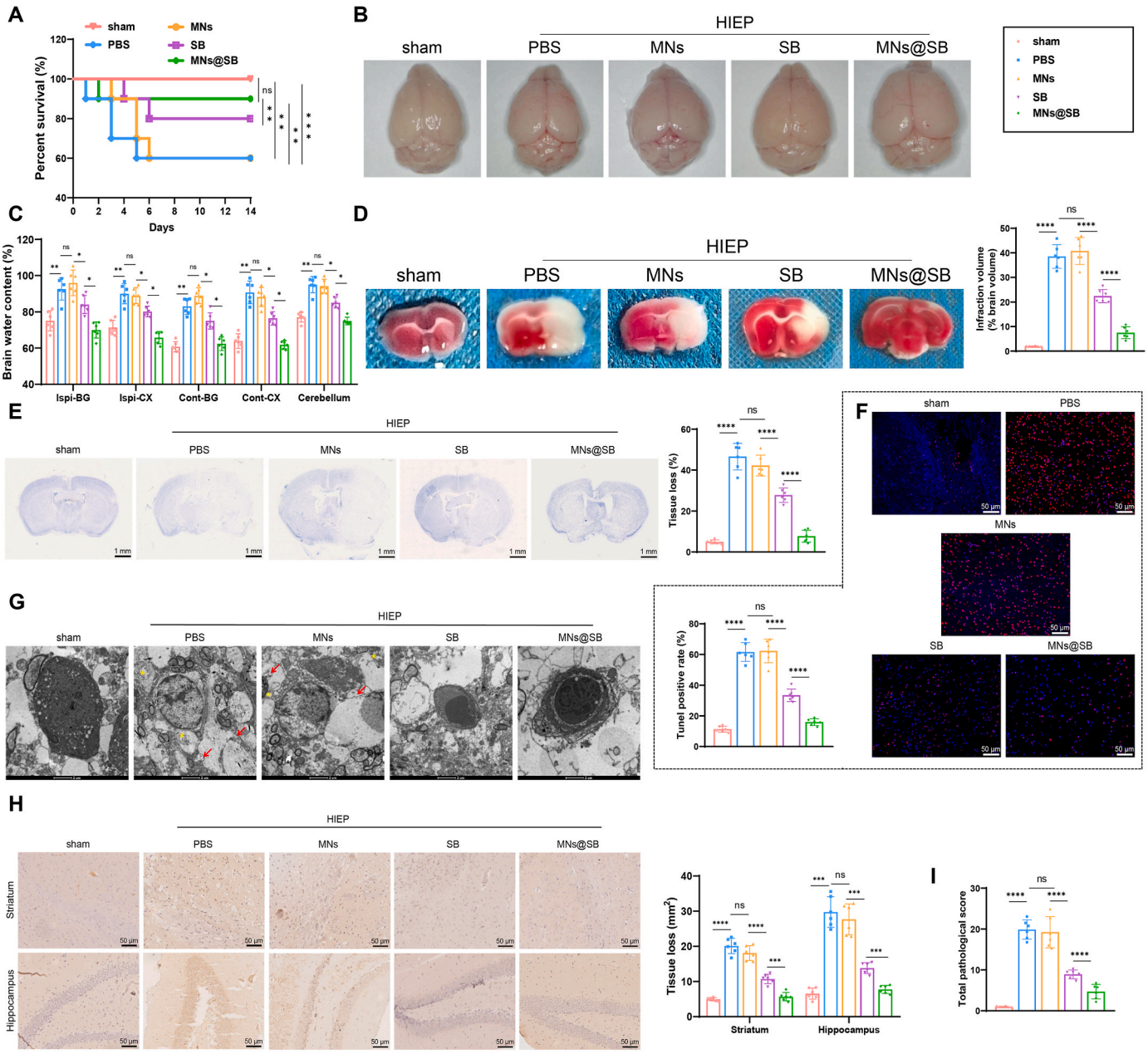

Fig. 4. Neurorepair Effects of MNs@SB on Brain Injury in HIEP Mice. Note: (A) Survival rates of HIEP mice under different drug treatments (n = 10); (B) Representative anatomical images of brains from different treatment groups of HIEP mice, with blue arrows indicating brain injury areas (n = 6); (C) Measurement of water content in different brain regions of HIEP mice from various treatment groups (n = 6); (D) TTC staining images of brains from different treatment groups of HIEP mice (n = 6); (E) Nissl staining images of brains from different treatment groups of HIEP mice (scale bar = 2 mm) (n = 6); (F) TUNEL staining detecting apoptosis in brain tissues from different treatment groups of HIEP mice (n = 6); (G) Representative TEM images of brain tissues from different treatment groups of HIEP mice, with red arrows indicating necrotic cells and yellow asterisks indicating swollen and vacuolated mitochondria (scale bar = 2 μm) (n = 6); (H) Immunohistochemical analysis of MAP2 expression in the striatum and hippocampus of brains from different treatment groups of HIEP mice, determining the area of damage (scale bar = 50 μm, n = 6); (I) Pathological scores of brain tissues from different groups of mice evaluated based on MAP2 staining results. Quantitative data are presented as Mean ± SD. Statistical significance between groups is indicated as follows: $^{*}p < 0.05$, $^{**}p < 0.01$, $^{***}p < 0.001$, $^{****}p < 0.0001$, with ns indicating no statistical difference.

neuropathological scoring further confirmed that HIEP-induced mice exhibited significant striatal and hippocampal volume loss and increased pathology scores compared to the sham group. The blank nanoparticle group showed no significant effect, while MNs@SB treatment reversed HIEP-induced brain damage. SB treatment alone provided moderate improvement but was less effective than MNs@SB, whereas MNs treatment alone did not mitigate brain damage (Fig. 4H–I).

Additionally, we performed HE staining to examine the morphology of the liver, kidneys, spleen, heart, and lung tissues of the mice. The results showed no significant changes in cell morphology or tissue structure in these major metabolic organs, further confirming the good biosafety of MNs@SB (Fig. S4).

In conclusion, our findings demonstrate that MNs@SB can significantly improve both short-term and long-term neurological deficits caused by HIEP and repair brain damage in HIEP mice.

3.4. Analysis of cellular heterogeneity and cell types in mouse brain tissue after MNs@SB treatment

To further investigate the impact of MNs@SB treatment on cellular heterogeneity in mouse brain tissue, we conducted scRNA-seq analysis on brain tissues from the MNs@SB treatment group (MNs@SB group, n = 1) and the control treatment group (PBS group, n = 1).

First, we integrated the sequencing data using the Seurat package and performed linear dimensional reduction using PCA. Batch correction was applied to the sample data using the harmony package (Figs. S5–S6). Next, we applied the t-SNE algorithm for nonlinear dimensional reduction of the top 20 PCs and used the "clustree" package to visualize the clustering at different resolutions (Fig. S7). Using t-SNE clustering analysis, we categorized all cells into ten distinct clusters (Fig. 5A–B). Subsequently, by referencing relevant literature, we identified known cell lineage-specific marker genes and annotated the cells using the online resource CellMarker. This resulted in the identification of six cell types: astrocytes, neurons, microglia, monocytes, T cells, and B cells (Fig. 5C–D). Additionally, we presented t-SNE expression maps for the marker genes of these six cell types: Gfap for astrocytes, NeuN for neurons, Iba1 for microglia, Cd11b for monocytes, Cd79a for T cells, and Cd3g for B cells (Fig. 5E–G).

Furthermore, we detailed the cellular composition distribution of the six identified cell types across the two samples. Using a T-test, we compared and analyzed the differences in cell numbers between the MNs@SB group and the PBS group. The results indicated that, compared to the PBS group, the MNs@SB group exhibited an increase in the number of neurons, microglia, and monocytes, with the most significant increase observed in neurons. Conversely, the number of astrocytes decreased (Fig. 5H).

The aforementioned scRNA-seq analysis results demonstrate that the brain tissue samples from mice in the MNs@SB and PBS groups can be classified into ten clusters, successfully identifying six cell subpopulations. Among these, the numbers of neurons, microglia, and monocytes increased, with neurons showing the most significant increase, while the number of astrocytes decreased.

3.5. Mechanism of MNs@SB action revealed by single-cell multi-omics sequencing

To further understand the functional differences underlying the observed cell number variations and to identify key cell types involved, we conducted pseudotime analysis using the "monocle" package. This analysis allowed us to order cells and construct trajectories based on gene expression trends (Fig. 6A). We found a significant accumulation of neurons at the end of branch node 3 during the later stages of cell differentiation (Fig. 6B–C). Thus, we hypothesize that neurons may play a crucial role in the repair of brain injury in HIEP mice treated with MNs@SB.

To further investigate the pivotal role of neurons in MNs@SB treatment, we studied intercellular communication mediated by ligand-receptor interactions. We used the "CellChat" package in R to analyze cell-to-cell communication and interaction between different cell phenotypes. The overall analysis revealed that, compared to the PBS group, the MNs@SB group exhibited an increase in both the number of pathway interactions and the communication strength between cells (Fig. 6D). Specifically, the connections between neurons and other cell types were enhanced in the MNs@SB samples compared to the PBS samples (Fig. 6E–F). The heatmap of interaction quantity and strength further demonstrated that the interaction intensity between neurons and other cells was significantly increased in the MNs@SB treatment group compared to the PBS group (Fig. 6G).

By comparing signaling pathways between the two groups, we identified both conserved and specific pathway differences. Analysis of signaling patterns in the cell communication networks showed that in the MNs@SB group, most cell types exhibited stronger outgoing and incoming signaling patterns, with neurons displaying the highest signaling intensity (Figs. S8A–C). Notably, the SPP1 pathway network showed a significantly increased activity in the MNs@SB samples (Fig. 6H). Furthermore, the interaction pathways between neurons and other cells indicated that, compared to the PBS samples, the strength and number of pathways involving neurons were significantly enhanced in the MNs@SB group (Figs. S8D–E). These results further underscore the critical role of neurons in the MNs@SB treatment process.

Additionally, we conducted a deeper analysis of the SPP1 signaling pathway. By constructing interaction networks of the SPP1 pathway between cells, we found that the signaling pathway was significantly enhanced among the six cell types in the brain tissue of MNs@SB group mice compared to the PBS group (Figs. S9A–D). The key molecules involved in the SPP1 signaling pathway in both PBS and MNs@SB samples are shown in Fig. S9E. These findings indicate that neurons are the pivotal cells mediating intercellular communication during MNs@SB treatment. Through these interactions, neurons may play a crucial role in brain repair and pathological processes following MNs@SB treatment.

To further investigate the key factors and signaling pathways mediated by neurons in brain repair after MNs@SB treatment, we extracted genes from neurons in the scRNA-seq dataset and conducted differential expression analysis. We identified 143 DEGs in neurons, with 71 genes upregulated and 72 genes downregulated in the MNs@SB group compared to the PBS group (Fig. 7A). Next, to identify key genes involved in MNs@SB treatment, we performed high-throughput transcriptome sequencing (Bulk RNA Sequencing, Bulk RNA-seq) on brain tissue samples from PBS group mice (n = 3) and MNs@SB group mice (n = 3). This analysis revealed 184 DEGs, including 129 upregulated and 55 downregulated genes (Fig. 7B–C).

We performed GO functional enrichment analysis on the DEGs identified from the Bulk RNA-seq data. The results showed that these genes were involved in several BP, including the transmembrane receptor protein serine/threonine kinase signaling pathway, BMP signaling pathway, and response to BMP. For CC, the genes were primarily enriched in the receptor complex, RNA polymerase II transcription regulator complex, and focal adhesion. In terms of MF, the genes were enriched in SMAD binding, transforming growth factor beta receptor binding, and I-SMAD binding (Fig. 7D–E).

Further KEGG pathway enrichment analysis revealed that these DEGs were mainly involved in the TGF-beta signaling pathway, Hippo signaling pathway, signaling pathways regulating pluripotency of stem cells, cell cycle, and cellular senescence, with a notable number of genes enriched in the TGF-beta signaling pathway (Fig. 7F–G). As shown in Fig. S10, the TGF-beta signaling pathway and related pathways were activated, with increased expression of TGF-beta signaling-related proteins in the treatment group compared to the PBS group.

By intersecting the DEGs from Bulk RNA-seq with the DEGs in neurons from scRNA-seq, we identified four common genes: Smad7, Olfml3, Tgfb1, and Sp1 (Fig. 7H). We used the GOSemSim package to calculate the semantic similarity of GO terms among these four intersecting genes. This analysis assesses the functional proximity of these genes by evaluating the shared GO terms. By comparing the functional similarity among genes, we can identify those that are functionally significant or anomalous. The results indicated that the Sp1 gene has the highest functional similarity (Fig. 7I), suggesting that Sp1 may play a central role in the relevant BP. The expression levels of these four intersecting genes in the Bulk RNA-seq dataset are shown in Fig. 7J, with Tgfb1 and Sp1 being upregulated in the treatment group, while Smad7 and Olfml3 are downregulated.

In summary, through the combined analysis of scRNA-seq and Bulk RNA-seq, we preliminarily identified neurons as the key cells mediating intercellular communication during MNs@SB treatment. The expression level of the Sp1 gene was significantly increased after MNs@SB treatment, suggesting its potential direct involvement in the physiological and pathological processes of brain injury repair. Furthermore, Sp1 may

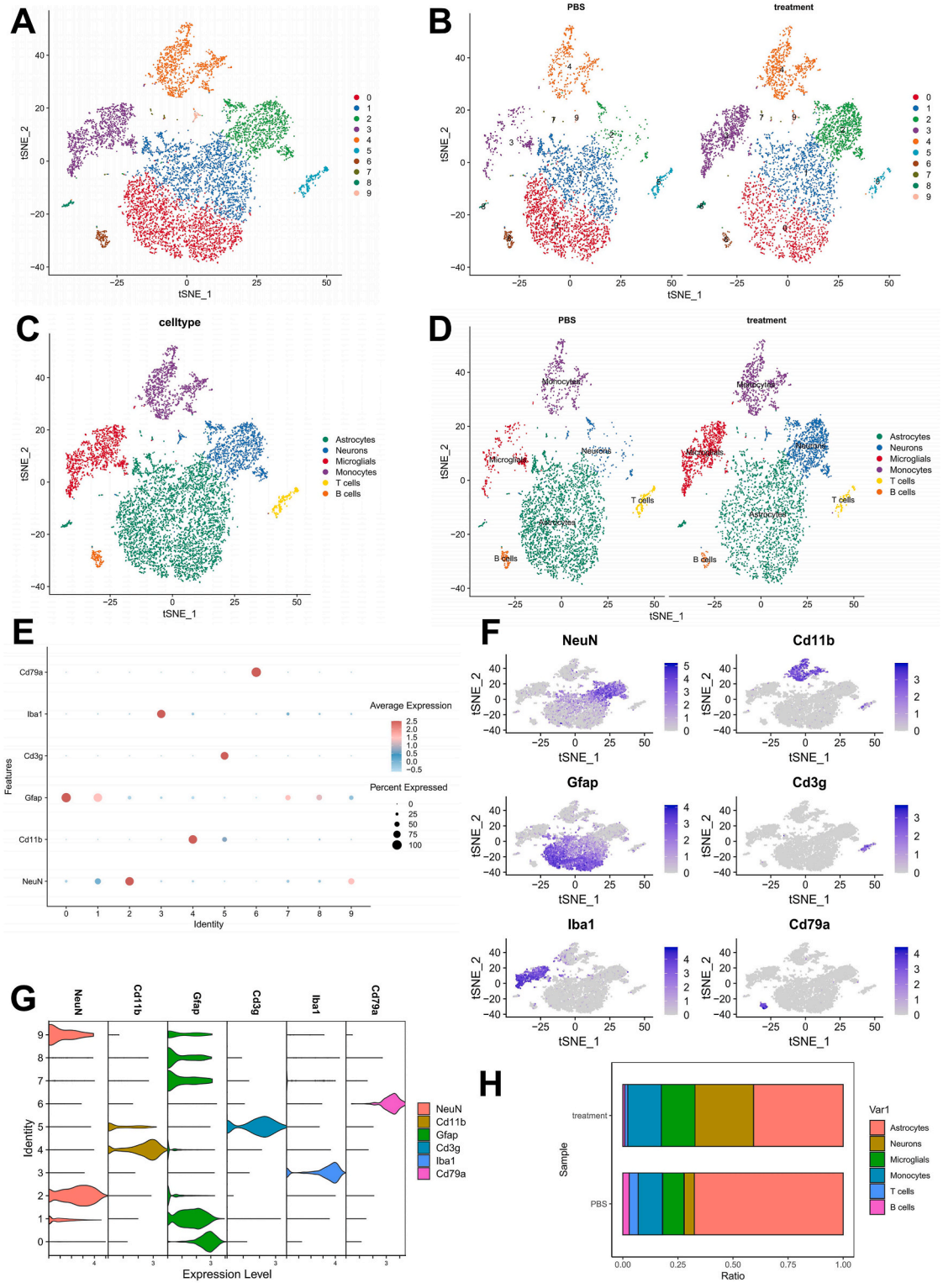

Fig. 5. Clustering of scRNA-seq Data. Note: (A) Visualization of t-SNE clustering results showing the aggregation and distribution of cells from different samples, with each color representing a cluster; (B) Visualization of t-SNE clustering results for cells from different samples, with each color representing a cluster; the left panel shows the PBS group, and the right panel shows the MNs@SB group; (C) Visualization of cell annotation results based on t-SNE clustering, with each color representing a cell subpopulation; (D) Visualization of cell annotation results based on t-SNE clustering, with each color representing a cell subpopulation; the left panel shows the PBS group, and the right panel shows the MNs@SB group; (E) Expression levels of known cell lineage-specific marker genes in different clusters from control and MNs@SB samples, with deeper red indicating higher average expression levels and larger circles representing more cells expressing the gene; (F) Expression levels of six cell marker genes in each cell subpopulation, with deeper blue indicating higher average expression levels; (G) Violin plots showing the expression levels of known cell lineage-specific marker genes in different clusters from control and MNs@SB samples; (H) Proportional representation of different cell subpopulations in each sample, with different colors indicating different cell subpopulation types.

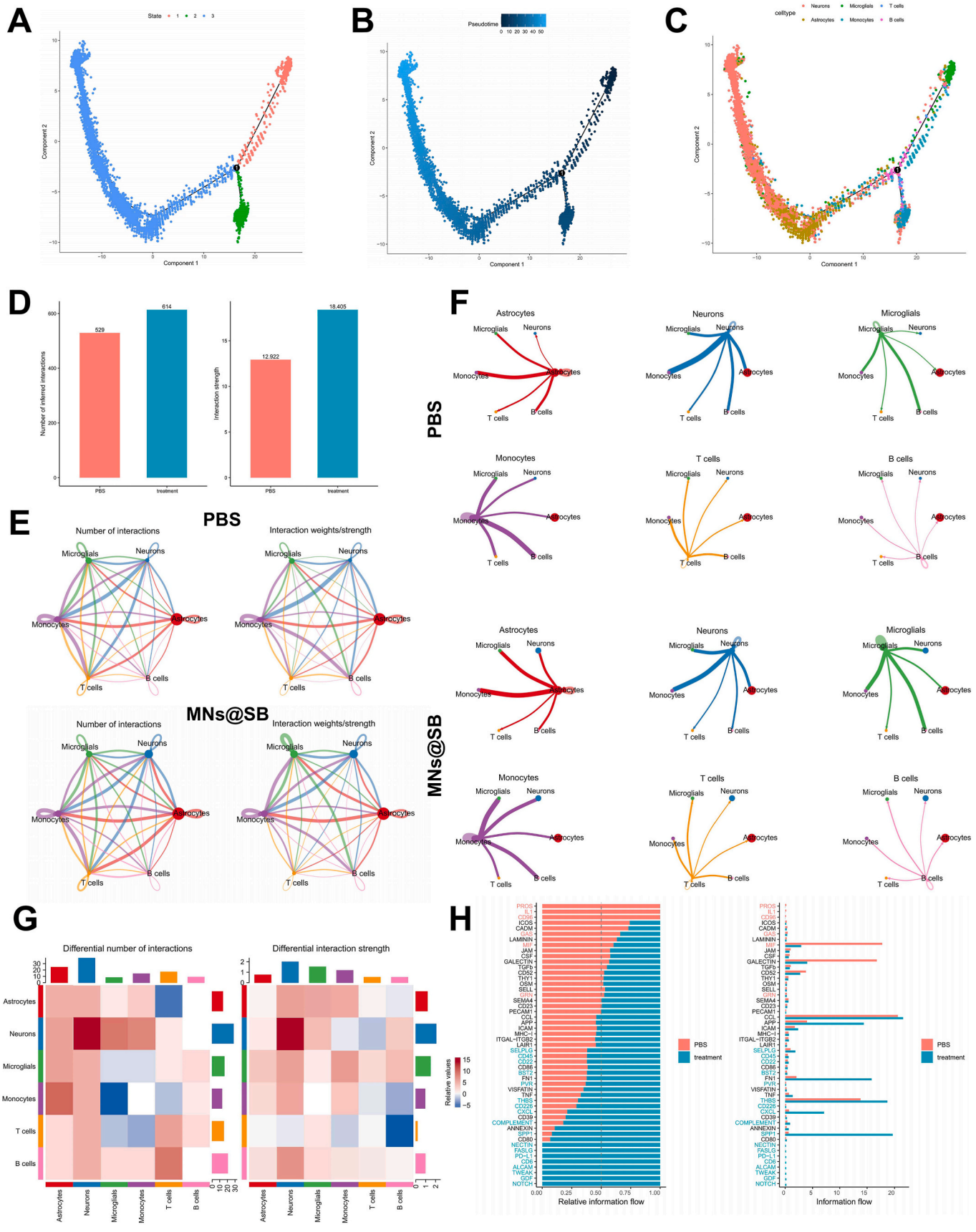

(caption on next page)

Fig. 6. Pseudotime Analysis and Cell Communication Analysis of Six Cell Types. Note: (A) Cell trajectory construction based on cell type and clustering, with trajectories built according to pseudotime; colors represent different cell clusters; (B) Cell trajectory construction based on cell type and clustering, with trajectories built according to pseudotime; colors transition from dark to light representing the progression of time; (C) Cell trajectory construction based on cell subpopulations, with each color representing a different cell subpopulation; (D) Comparison of the total number of pathway interactions and interaction strength between PBS and MNs@SB samples (PBS, n = 1; MNs@SB, n = 1); (E) Circle plots of cell communication in PBS and MNs@SB samples, with line thickness representing the number of pathways and interaction strength; (F) Circle plots showing interactions between each of the six cell types and the other five cell types in PBS and MNs@SB samples, with line thickness representing the number of pathways; (G) Heatmap comparing the number of pathway interactions (left) and interaction strength (right) between the six cell types in PBS and MNs@SB samples; red indicates enhanced interactions, blue indicates reduced interactions, with deeper colors representing more significant changes; (H) Comparison of conserved and specific pathways involved in PBS and MNs@SB groups, with the horizontal axis representing outgoing signals and the vertical axis representing incoming signals.

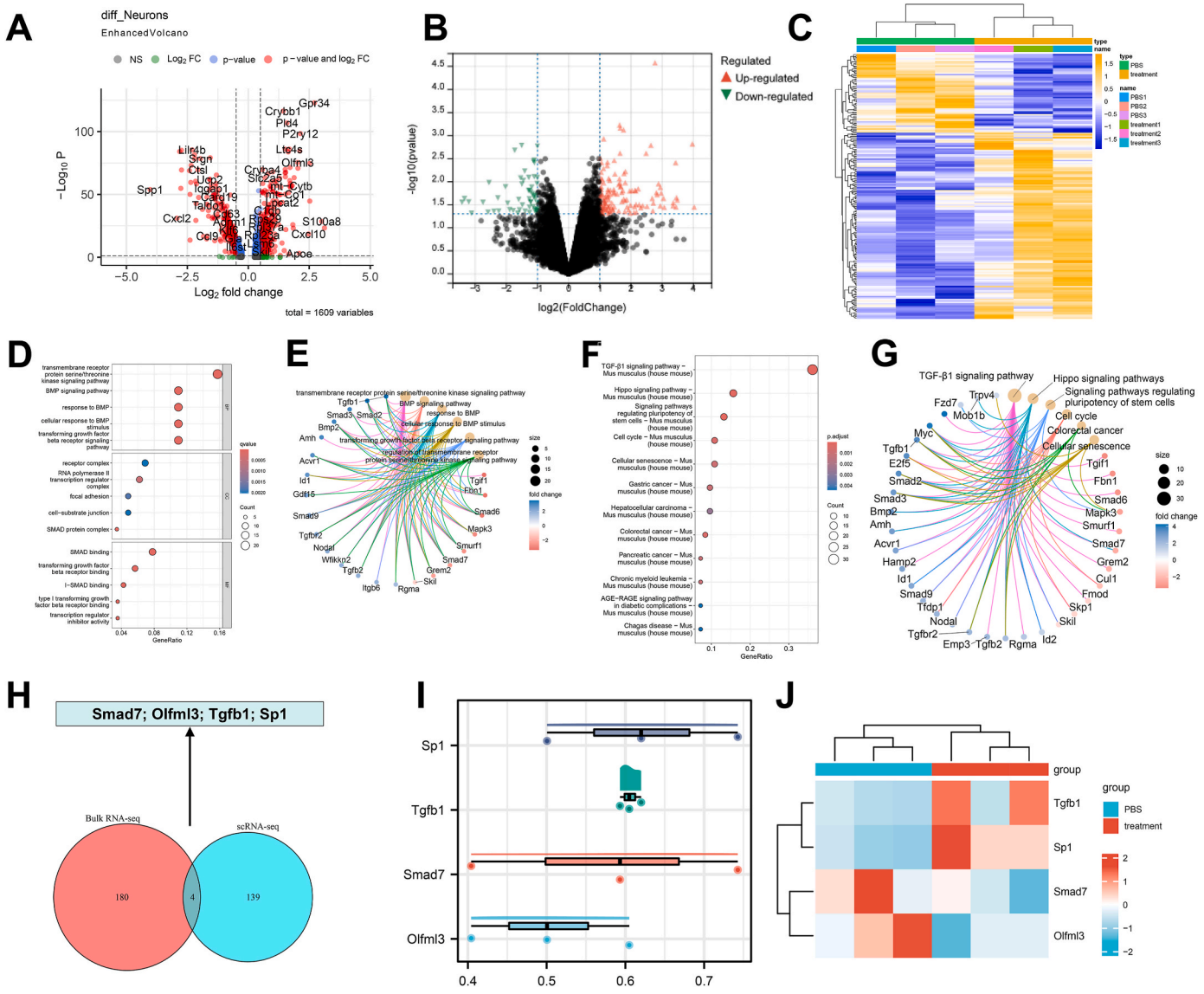

Fig. 7. Screening of Key Genes through scRNA-seq and Bulk RNA-seq Analysis. Note: (A) Volcano plot of DEGs in neurons from PBS and MNs@SB samples, with red dots to the right of the dashed line representing upregulated genes in the MNs@SB group, and dots to the left representing downregulated genes in the MNs@SB group; (B) Volcano plot of DEGs from Bulk RNA-seq of three PBS and three MNs@SB samples, with red triangles representing upregulated genes, green inverted triangles representing downregulated genes, and black dots representing non-differential genes; (C) Heatmap of DEGs from Bulk RNA-seq of three PBS and three MNs@SB samples, with yellow representing upregulation and blue representing downregulation, with deeper colors indicating more significant differences; (D) Bubble plot of GO enrichment analysis of DEGs from Bulk RNA-seq, with circle color representing the significance of enrichment from blue to red and circle size representing the number of enriched genes; (E) Circle plot of GO enrichment analysis of DEGs from Bulk RNA-seq; (F) Bubble plot of KEGG enrichment analysis of DEGs from Bulk RNA-seq, with circle color representing the significance of enrichment from blue to red and circle size representing the number of enriched genes; (G) Circle plot of KEGG enrichment analysis of DEGs from Bulk RNA-seq; (H) Venn diagram showing the intersection of DEGs from Bulk RNA-seq and DEGs in neurons from scRNA-seq; (I) GO semantic similarity analysis of the four intersecting genes; (J) Heatmap of the expression of the four intersecting genes, with red indicating upregulation and blue indicating downregulation, with deeper colors indicating more significant differences.

promote the repair of brain injury in HIEP mice by activating the TGF-β1 signaling pathway.

3.6. Further confirmation that MNs@SB promotes brain repair by upregulating Sp1 and activating the TGF-β1 signaling pathway

To further investigate whether MNs@SB promotes the repair of HIEP-induced brain injury through Sp1, we examined the expression of the neuronal marker protein NSE in the brain tissues of mice from different treatment groups. The results showed that, compared to the sham group, the expression of NSE protein was significantly reduced in HIEP mice (PBS group). However, after MNs@SB treatment, the number of neurons in the brain tissue significantly increased (Fig. 8A).

We also examined the changes in SP1 mRNA and protein expression in the brain tissues of mice from different treatment groups. The results indicated that, compared to the sham group, the expression of SP1 mRNA and protein was significantly decreased in the PBS group. Conversely, after MNs@SB treatment, the expression of SP1 mRNA and

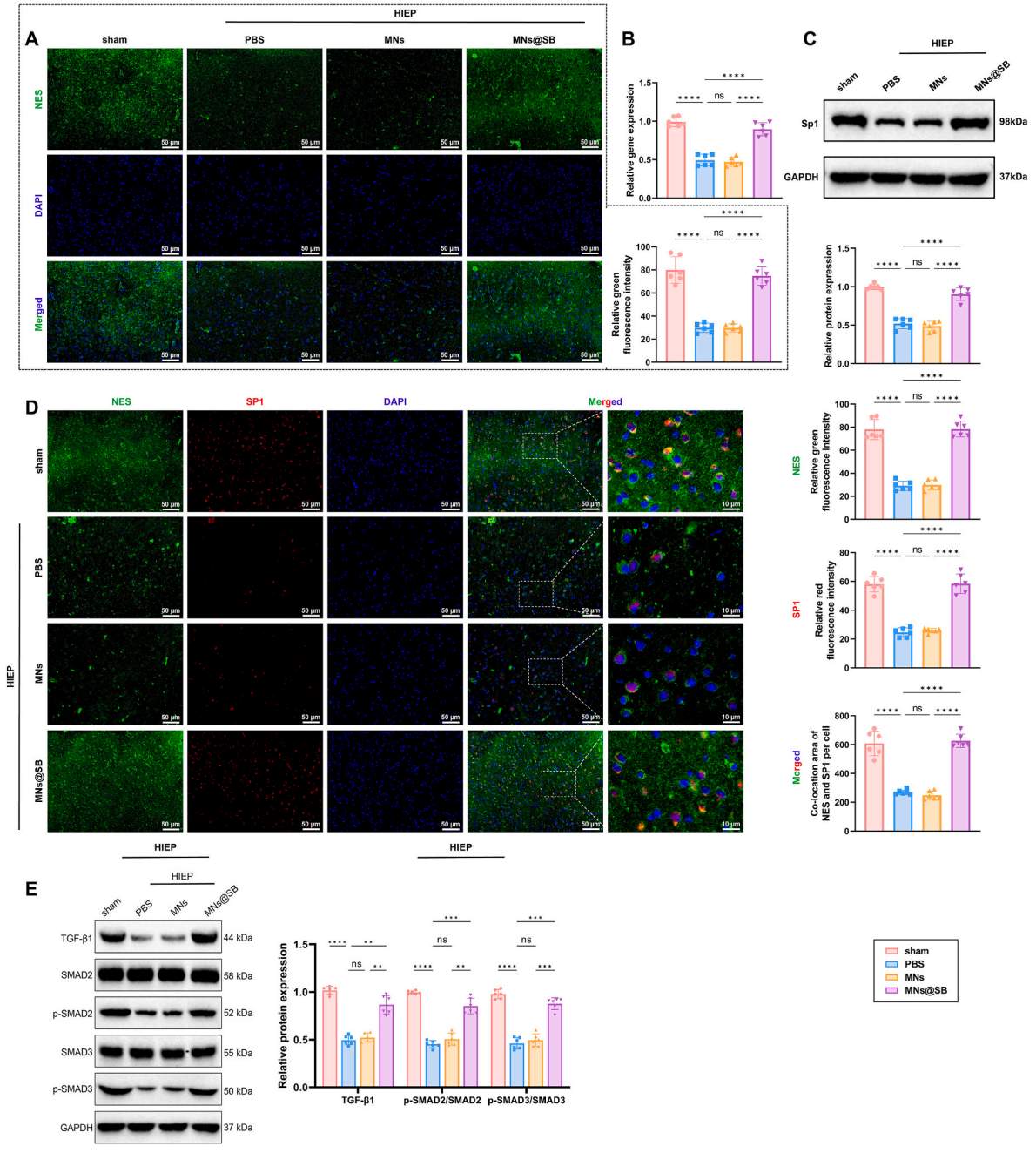

Fig. 8. MNs@SB Upregulates Sp1 to Activate the TGF-β1 Signaling Pathway and Promote Brain Repair in HIEP Mice. Note: (A) Immunofluorescence staining showing changes in NES protein expression in mouse brain tissues from different treatment groups; green fluorescence indicates NES protein and blue fluorescence indicates DAPI nuclear staining (scale bar: 50 μm); (B) RT-qPCR analysis of Sp1 mRNA expression in mouse brain tissues from different treatment groups; (C) Western blot analysis of SP1 protein expression in mouse brain tissues from different treatment groups; (D) Immunofluorescence staining showing changes in NES protein expression in mouse brain tissues from different treatment groups, with green fluorescence for NES protein, red fluorescence for SP1 protein, and blue fluorescence for DAPI nuclear staining (scale bar: 100/50 μm); (E) Western blot analysis of TGF-β1, SMAD2, p-SMAD2, SMAD3, and p-SMAD3 protein expression in mouse brain tissues from different treatment groups. Quantitative data are presented as Mean ± SD, with each group consisting of six mice. Statistical significance between groups is indicated as follows: $^{**}p < 0.01$, $^{***}p < 0.001$, $^{****}p < 0.0001$, with ns indicating no statistical difference.

protein was restored in the brain tissues of the mice (Fig. 8B–C). These findings confirm that MNs@SB can upregulate the expression of SP1 in neurons. Immunofluorescence staining further validated these results (Fig. 8D).

Western blot analysis showed that HIEP-induced brain injury significantly reduced the levels of TGF-β1, p-SMAD2, and p-SMAD3 proteins in mouse brain tissue. However, MNs@SB treatment significantly restored the expression of TGF-β1, p-SMAD2, and p-SMAD3 proteins, indicating that MNs@SB treatment activated the TGF-β1/SMAD2/3 signaling pathway (Fig. 8E).

To further investigate the regulatory role of Sp1 on neuronal biological characteristics, we extracted neurons from mouse brain tissue. As shown in Fig. S11A, on the 8th day of growth, neurons displayed typical morphology with clear cell bodies and long axons extending from both sides, forming a network. By the 11th day, neuronal networks had expanded, and neurite outgrowth had increased. After 11 days of growth, neurons were fixed and stained with the neuronal marker NSE. As seen in Fig. S11B, NSE antibody staining was positive, confirming that the cultured cells were indeed neurons.

To further validate the impact of the Sp1 gene on neuronal proliferation and apoptosis, we designed three shRNA sequences targeting Sp1 and constructed Sp1-silenced neurons through lentiviral

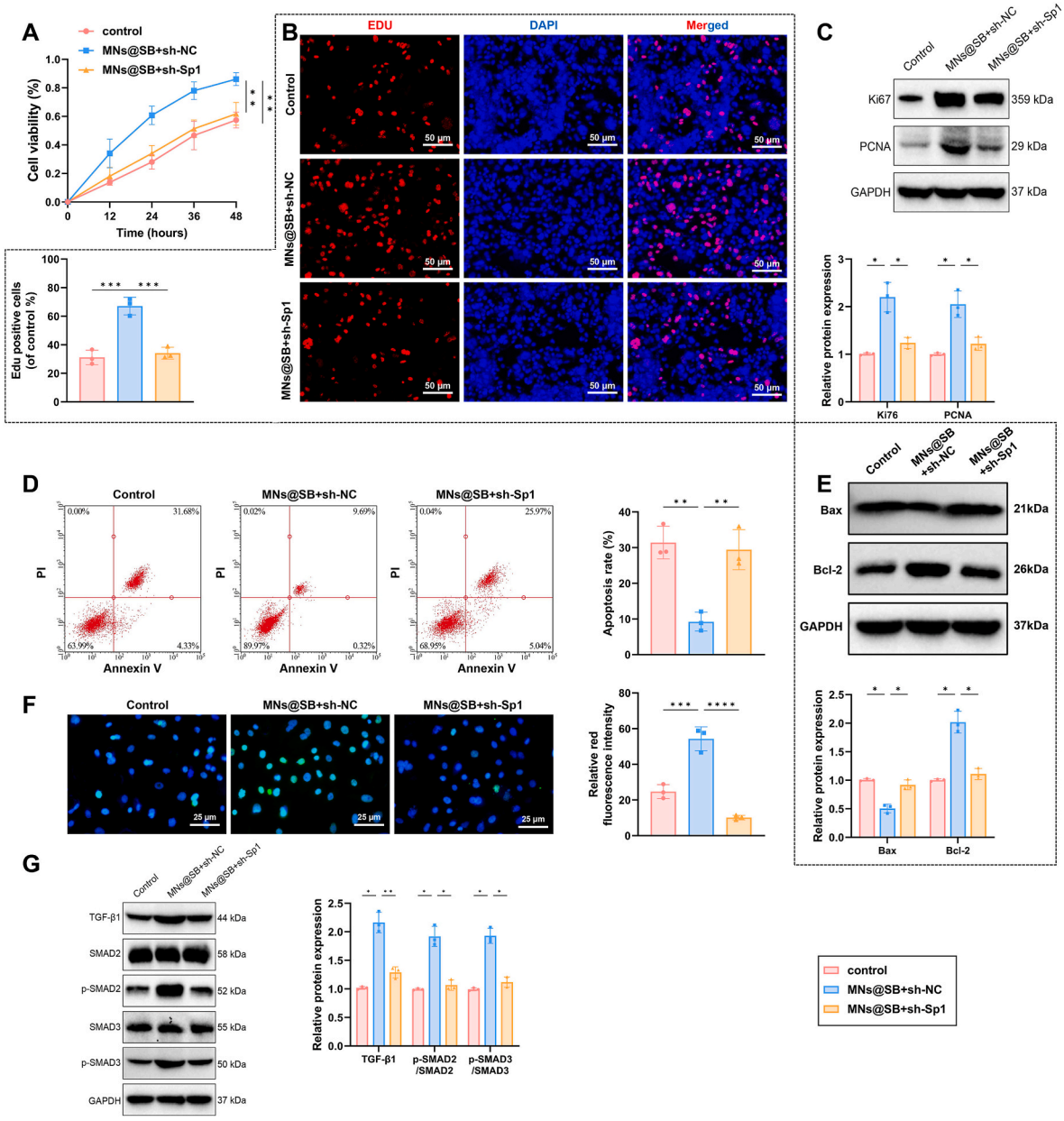

Fig. 9. MNs@SB Upregulates Sp1 to Activate the TGF-β1 Signaling Pathway and Inhibit Neuronal Apoptosis. Note: (A) CCK-8 assay detecting changes in neuronal viability at 12, 24, 36, and 48 h across different treatment groups; (B) EdU assay detecting neuronal proliferation in different treatment groups, with EdU-positive cells in red indicating proliferating cells and blue DAPI staining indicating nuclei (scale bar = 25 μm); (C) Western blot analysis of Ki67 and PCNA protein expression in neurons from different treatment groups; (D) AnnexinV/PI double staining flow cytometry analysis of neuronal apoptosis in different treatment groups, with the histogram showing the apoptosis rate as the sum of cells in Q2 and Q3 quadrants; (E) Western blot analysis of Bax and Bcl-2 protein expression in neurons from different treatment groups; (F) Immunofluorescence staining detecting SP1 protein expression in neurons from different treatment groups, with green fluorescence indicating SP1 protein and blue DAPI staining indicating nuclei (scale bar: 50 μm); (G) Western blot analysis of TGF-β1, SMAD2, p-SMAD2, SMAD3, and p-SMAD3 protein expression in neurons from different treatment groups. Quantitative data are presented as Mean ± SD, with each experiment repeated three times per group. Statistical significance between groups is indicated as follows: *$p < 0.05$, **$p < 0.01$, ***$p < 0.001$, ****$p < 0.0001$.

transfection. The transfection efficiency was confirmed using RT-qPCR and Western blot, with the most effective sequence, sh-Sp1-3 (hereafter referred to as sh-Sp1), selected for subsequent experiments (Fig. S12). SP1 immunofluorescence staining further confirmed the silencing efficiency of SP1 (Figs. S13A–B).

The results of CCK-8 and EdU assays indicated that silencing SP1 in neurons significantly reduced cell viability and proliferation capacity (Figs. S13C–D). Additionally, the expression of the cell proliferation markers Ki67 and PCNA was markedly decreased, further confirming that silencing Sp1 inhibits neuronal proliferation (Fig. S13E). Flow cytometry analysis revealed that silencing SP1 induced an increase in neuronal apoptosis (Fig. S13F). In Sp1-silenced neurons, the expression of the pro-apoptotic protein Bax was increased, while the expression of the anti-apoptotic protein Bcl-2 was significantly reduced (Fig. S13G). Moreover, Western blot analysis showed that, compared to the sh-NC group, the expression of TGF-β1, p-SMAD2, and p-SMAD3 proteins in Sp1-silenced neurons was significantly decreased, indicating inhibition of the TGF-β1 signaling pathway (Fig. S13H).

To further verify that the NPs MNs@SB activate the TGF-β1 signaling pathway through Sp1, we constructed an *in vitro* ischemic-hypoxic neuron model using a specialized hypoxia incubator and the OGD method. This model was then treated with MNs@SB. The results showed that MNs@SB increased the viability and proliferation capacity of ischemic-hypoxic neurons and promoted the expression of Ki67 and PCNA proteins. However, silencing Sp1 reversed the regulatory effects of MNs@SB on neuronal cell viability and proliferation (Fig. 9A–C). Furthermore, MNs@SB inhibited apoptosis in ischemic-hypoxic neurons by decreasing Bax protein expression and increasing Bcl-2 protein expression. Silencing Sp1 also reversed these effects of MNs@SB (Fig. 9D–E).

Moreover, MNs@SB treatment promoted the expression of SP1, TGF-β1, p-SMAD2, and p-SMAD3 proteins in ischemic-hypoxic neurons. Silencing Sp1 subsequently downregulated the expression of these proteins (Fig. 9F–G).

These findings demonstrate that MNs@SB enhances the expression of Sp1 in neurons, which in turn activates the TGF-β1 signaling pathway. This activation inhibits neuronal apoptosis and promotes brain repair in HIEP mice.

4. Discussion

HIEP is a major cause of acute mortality and chronic neurological damage in premature infants. Current treatment approaches primarily focus on supportive and symptomatic care, lacking effective neuroregenerative interventions [62–64]. In recent years, SB, a SCFA, has garnered significant attention for its potential role in neuroprotection and repair [65]. However, the targeted delivery and stability of SB in the brain remain significant challenges. This study aims to achieve efficient treatment of HIEP by designing and synthesizing MNs@SB. Compared to traditional treatments, this research utilizes nanotechnology and magnetic targeting strategies to enhance the stability and targeting of SB. Additionally, FUS is employed to facilitate drug diffusion in the brain, providing an innovative therapeutic approach [66–68].

In this study, the design of MNs@SB is based on its dual functions of magnetic targeting and fluorescent labeling, ensuring precise *in vivo* localization and real-time monitoring. We synthesized MNs containing SB and conducted a series of *in vitro* and *in vivo* experiments to verify their magnetic targeting efficacy and biosafety. Compared to other NP systems used in previous studies, MNs@SB offers significant advantages in terms of targeting and stability. For instance, while prior research primarily employed electrostatic adsorption or chemical bonding methods for drug loading, MNs@SB utilizes magnetic targeting technology for more efficient drug delivery [69,70]. Additionally, the fluorescent labeling of MNs@SB enhances its performance in *vivo* imaging and drug release monitoring, providing a real-time, visual assessment of therapeutic efficacy.

Butyrate, an important short-chain fatty acid, has been shown to play a crucial role in maintaining gut health and regulating immune responses [71]. Based on previous studies, sodium butyrate is speculated to be a key mediator in the "gut-microbiota-brain" axis, providing a novel therapeutic target for HIEP by inhibiting neuronal apoptosis and promoting neural repair [72,73]. However, the precise mechanisms of butyrate in the "gut-microbiota-brain" axis remain unclear [74–76]. We hypothesize that in HIEP mice (a model possibly related to hypoxic-ischemic encephalopathy), certain gene expression changes may impact butyrate metabolism pathways. For example, the transcription of genes associated with key enzymes involved in butyrate metabolism may be downregulated. Butyrate metabolism involves multiple enzymes, such as butyryl-CoA dehydrogenase, whose gene promoters could be methylated or inhibited by transcriptional repressors, leading to reduced gene expression [77]. Additionally, hypoxia-ischemia may result in excessive production of reactive oxygen species (ROS) and inflammatory mediators, which can disrupt the normal metabolic environment within cells. These factors may oxidatively damage butyrate-metabolizing enzymes, reducing their activity. Moreover, inflammatory mediators could activate specific signaling pathways, such as the NF-κB pathway, triggering cellular stress responses that further suppress butyrate metabolism [78,79]. Using untargeted metabolomics sequencing, this study found that the butyrate metabolism pathway was significantly inhibited in the intestines of HIEP mice. Our results suggest that hypoxic-ischemic injury may disturb gut microbiota composition, thereby reducing butyrate production and leading to gut-brain axis dysfunction. This dysregulation could exacerbate neuroinflammation and delay neural repair. For the first time, this study proposes that suppression of the butyrate metabolism pathway may be a critical metabolic alteration in the pathological process of HIEP. Unlike previous research that primarily focused on butyrate's role in the gut, our study further explores its potential in brain injury repair.

This study demonstrated through *in vivo* and *in vitro* experiments that MNs@SB can significantly repair brain damage in HIEP mice and improve their short-term and long-term neurological deficits. *In vitro* experiments showed that MNs@SB exhibited excellent magnetic targeting and biosafety. *In vivo*, after tail vein injection, MNs@SB was magnetically targeted to the brain and, with the assistance of FUS, achieved effective drug diffusion within the brain. Compared to traditional drugs and other NP-based therapies, MNs@SB showed higher efficiency and safety in repairing neural damage [80,81]. For instance, traditional drugs often struggle to effectively reach the brain due to the BBB. In contrast, MNs@SB successfully overcame this barrier through magnetic targeting, achieving precise drug delivery and significant therapeutic effects. The uptake of MNs@SB nanoparticles by neurons involved receptor-mediated endocytosis. In our study, Fe3O4 nanoparticles were surface-modified with PEG and DOPA, which enhanced cellular uptake by facilitating interactions with membrane lipid rafts. Additionally, FUS temporarily opened the cell membrane, promoting nanoparticle entry.

Using scRNA-seq and high-throughput transcriptomics sequencing, this study identified neurons as the key cells mediating the therapeutic effects of MNs@SB. Further analysis highlighted the critical roles of the key gene Sp1 and the TGF-β1 signaling pathway in HIEP treatment. Sp1, a transcription factor, has been extensively studied for its regulatory role in apoptosis and proliferation, while the TGF-β1 signaling pathway is known to play crucial roles in cell growth, differentiation, and immune regulation. Unlike previous studies that focused solely on Sp1 or TGF-β1, this research systematically elucidates the mechanism by which MNs@SB upregulates Sp1 in neurons, thereby activating the TGF-β1 signaling pathway. This activation inhibits neuronal apoptosis and promotes brain injury repair. By integrating scRNA-seq with *in vitro* and *in vivo* experiments, this study provides a comprehensive understanding of how MNs@SB exerts its therapeutic effects, offering significant insights into the pathological mechanisms of HIEP and laying the groundwork for the development of novel therapeutic strategies.

In summary, this study utilized scRNA-seq sequencing combined with high-throughput transcriptome sequencing to identify neurons as the key cells mediating the intercellular communication effects of MNs@SB treatment. Further analysis highlighted Sp1 as a critical gene associated with neurons and the TGF-β1 signaling pathway as a significant functional pathway. *In vivo* and *in vitro* analyses confirmed that MNs@SB treatment upregulates Sp1 in neurons, activates the TGF-β1 signaling pathway, inhibits neuronal apoptosis, and thereby promotes brain injury repair in HIEP mice.

This study developed MNs@SB and demonstrated its neurorepair effects in HIEP, revealing the critical role of SB in regulating the Sp1 and TGF-β1 signaling pathways. The scientific value lies in the first systematic analysis of neuronal apoptosis and repair mechanisms in a HIEP mouse model using scRNA-seq and high-throughput transcriptomics technologies, expanding our understanding of the gut-brain axis in neurological diseases. Clinically, this study provides an innovative and precise therapeutic strategy that employs magnetic targeting and FUS techniques to achieve efficient delivery of SB across the BBB, significantly improving neurological deficits in HIEP mice. This approach brings new hope and direction for the treatment of HIEP in preterm infants.

Despite the significant experimental results achieved in this study, several limitations remain. Firstly, the small sample size may affect the generalizability and statistical significance of the results. Secondly, the research primarily focused on animal models, lacking data from human clinical trials. Thus, the specific efficacy and safety of MNs@SB in human patients remain unclear. Premature infants, particularly neonates, are highly vulnerable, necessitating extreme caution when introducing biomaterials into their systems. Since magnetic nanoparticles contain iron ions, excessive metabolism of these materials *in vivo* may increase the risk of hyperferritinemia in preterm infants. In future studies, we aim to optimize alternative nanomaterials to mitigate iron-related interference. Additionally, the absence of long-term follow-up data limits the assessment of the long-term effects and potential side effects of MNs@SB. While our results indicate no significant differences in therapeutic efficacy over varying treatment durations, further investigations are required to explore potential drug tolerance or cumulative side effects over extended treatment periods, such as six months, one year, or longer (~34 weeks, [82]. Lastly, the complex synthesis and high cost of NPs may restrict their large-scale application in clinical settings.

Future research should focus on further optimizing the design of MNs@SB to enhance its drug delivery efficiency and biocompatibility while reducing production costs. It is also essential to expand the scale of preclinical studies, utilizing multi-center large sample experiments to validate its efficacy and safety, thereby laying the groundwork for clinical trials. Long-term follow-up studies are particularly needed to evaluate the long-term effects and potential side effects of MNs@SB in treating HIEP. Additionally, exploring the combined use of MNs@SB with other therapeutic methods in clinical trials could potentially uncover more effective comprehensive treatment strategies, providing more options and better outcomes for the treatment of HIEP in preterm infants.

CRediT authorship contribution statement

Jing Zhao: Conceptualization. **Jun Zhang:** Conceptualization. **Li Hou:** Conceptualization. **Can Yang:** Conceptualization. **Lin Jiang:** Conceptualization. **Daoxin Liang:** Conceptualization.

Ethical statement

All animal experiments were approved by the Animal Ethics Committee of Affiliated Hospital of North Sichuan Medical College.

Funding

This study was supported by Sichuan Provincial Medical Research Project (S23002), Nanchong University Cooperation-National Natural Science Foundation of China Pre-Research Project (20SXZRKX0003), Sichuan North Medical College Provincial Scientific Research Project Cultivation (CBY22-ZDA04).

Declaration of competing interest

The authors declare that they have no known competing financial interests or personal relationships that could have appeared to influence the work reported in this paper.

Acknowledgment

None.

Abbreviations

BBB	Blood-Brain Barrier
BP	Biological Process
CC	Cellular Component
CCK-8	Cell Counting Kit-8
Cont-BG	Contralateral Basal Ganglia
Cont-CX	Contralateral Cerebral Cortex
DEGs	Differentially Expressed Genes
DMs	Differential Metabolites
FUS	Focusing Ultrasound
GC/MS	Gas Chromatography-Mass Spectrometry
GO	Gene Ontology
H&E	Hematoxylin and Eosin
HIE	Hypoxic-Ischemic Encephalopathy
HIEP	Hypoxic-Ischemic Encephalopathy of Prematurity
Ipsi-BG	Ipsilateral Basal Ganglia
Ipsi-CX	Ipsilateral Cortex
KEGG	Kyoto Encyclopedia of Genes and Genomes
MF	Molecular Functions
MNs@SB	Magnetic Fluorescent Nanoparticles Loaded with Sodium Butyrate
MWMT	Morris Water Maze Test
NORT	Novel Object Recognition Test
NSE	Neurospecific Enolase
NTA	Nanoparticle Tracking Analysis
NPs	Nanoparticles
OGD	Oxygen-Glucose Deprivation
PCA	Principal Component Analysis
PCoA	Principal Coordinates Analysis
PCs	Principal Components
PLS-DA	Partial Least Squares Discriminant Analysis
PTFE	Polytetrafluoroethylene
RT-qPCR	Reverse Transcription Quantitative Polymerase Chain Reaction
SB	Sodium Butyrate
SCFA	Short-Chain Fatty Acid
TEM	Transmission Electron Microscopy
TH	Therapeutic Hypothermia
t-SNE	t-Distributed Stochastic Neighbor Embedding
XRD	X-Ray Diffraction

Appendix A. Supplementary data

Supplementary data to this article can be found online at https://doi.org/10.1016/j.mtbio.2025.101665.

Data availability

Data will be made available on request.

References

[1] J.B. Russ, R. Simmons, H.C. Glass, Neonatal encephalopathy: beyond hypoxic-ischemic encephalopathy, NeoReviews 22 (2021) e148–e162, https://doi.org/10.1542/neo.22-3-e148.

[2] Y. Li, J.L. Wisnowski, L. Chalak, A.M. Mathur, R.C. McKinstry, G. Licona, D. E. Mayock, T. Chang, K.P. Van Meurs, T.-W. Wu, K.A. Ahmad, M.-C. Cornet, R. Rao, A. Scheffler, Y.W. Wu, Mild hypoxic-ischemic encephalopathy (HIE): timing and pattern of MRI brain injury, Pediatr. Res. 92 (2022) 1731–1736, https://doi.org/10.1038/s41390-022-02026-7.

[3] S.L. Bonifacio, S. Hutson, The term newborn, Clin. Perinatol. 48 (2021) 681–695, https://doi.org/10.1016/j.clp.2021.05.014.

[4] R.L. Hoiland, C. Robba, D.K. Menon, G. Citerio, C. Sandroni, M.S. Sekhon, Clinical targeting of the cerebral oxygen cascade to improve brain oxygenation in patients with hypoxic–ischaemic brain injury after cardiac arrest, Intensive Care Med. 49 (2023) 1062–1078, https://doi.org/10.1007/s00134-023-07165-x.

[5] R. Narayanamurthy, J.-L.J. Yang, J.Y. Yager, L.D. Unsworth, Drug delivery platforms for neonatal brain injury, J. Contr. Release 330 (2021) 765–787, https://doi.org/10.1016/j.jconrel.2020.12.056.

[6] N. Labusek, Y. Mouloud, C. Köster, E. Diesterbeck, T. Tertel, C. Wiek, H. Hanenberg, P.A. Horn, U. Felderhoff-Müser, I. Bendix, B. Giebel, J. Herz, Extracellular vesicles from immortalized mesenchymal stromal cells protect against neonatal hypoxic-ischemic brain injury, Inflamm. Regen. 43 (2023), https://doi.org/10.1186/s41232-023-00274-6.

[7] T. Arnautovic, S. Sinha, A.R. Laptook, Neonatal hypoxic-ischemic encephalopathy and hypothermia treatment. Obstetrics & Gynecology, 2023, https://doi.org/10.1097/aog.0000000000005392.

[8] H.C. Glass, A.L. Numis, B.A. Comstock, F.F. Gonzalez, U. Mietzsch, S.L. Bonifacio, S. Massey, C. Thomas, N. Natarajan, D.E. Mayock, G.M. Sokol, K.P. Van Meurs, K. A. Ahmad, N. Maitre, P.J. Heagerty, S.E. Juul, Y.W. Wu, C.J. Wusthoff, Association of EEG background and neurodevelopmental outcome in neonates with hypoxic-ischemic encephalopathy receiving hypothermia, Neurology 101 (2023), https://doi.org/10.1212/wnl.0000000000207744.

[9] J.O. Davidson, F. Gonzalez, P. Gressens, A.J. Gunn, Update on mechanisms of the pathophysiology of neonatal encephalopathy, Semin. Fetal Neonatal Med. 26 (2021) 101267, https://doi.org/10.1016/j.siny.2021.101267.

[10] B. Luo, H. Zhou, Y. Sun, Q. Xiao, L. Chen, H. She, S. Wang, S. Yan, Q. Chang, Y. He, L. Xiong, The fate and prospects of stem cell therapy in the treatment of hypoxic–ischemic encephalopathy, Eur. J. Neurosci. 58 (2023) 2384–2405, https://doi.org/10.1111/ejn.16040.

[11] Y.-K. Lin, S. Hwang-Bo, Y.-M. Seo, Y.-A. Youn, Clinical seizures and unfavorable brain MRI patterns in neonates with hypoxic ischemic encephalopathy, Medicine 100 (2021) e25118, https://doi.org/10.1097/md.0000000000025118.

[12] M.-A. Fitzcharles, S.P. Cohen, D.J. Clauw, G. Littlejohn, C. Usui, W. Häuser, Nociplastic pain: towards an understanding of prevalent pain conditions, Lancet 397 (2021) 2098–2110, https://doi.org/10.1016/s0140-6736(21)00392-5.

[13] Z.A. Sherif, C.R. Gomez, T.J. Connors, T.J. Henrich, W.B. Reeves, Pathogenic mechanisms of post-acute sequelae of SARS-CoV-2 infection (PASC), Elife 12 (2023), https://doi.org/10.7554/elife.86002.

[14] S.J. Mann, J.C. Lam, P. Singh, McKenzie back exercises, in: StatPearls, StatPearls Publishing, Treasure Island (FL), 2023.

[15] X. Du, D. Kong, R. Guo, B. Liu, J. He, J. Zhang, A.E. Amponsah, H. Cui, J. Ma, Combined transplantation of hiPSC-NSC and hMSC ameliorated neuroinflammation and promoted neuroregeneration in acute spinal cord injury, Stem Cell Res. Ther. 15 (2024), https://doi.org/10.1186/s13287-024-03655-x.

[16] A. Góralczyk-Bińkowska, D. Szmajda-Krygier, E. Kozłowska, The microbiota–gut–brain Axis in psychiatric disorders, IJMS 23 (2022) 11245, https://doi.org/10.3390/ijms231911245.

[17] E.A. Mayer, K. Nance, S. Chen, The gut–brain Axis, Annu. Rev. Med. 73 (2022) 439–453, https://doi.org/10.1146/annurev-med-042320-014032.

[18] K. Socała, U. Doboszewska, A. Szopa, A. Serefko, M. Włodarczyk, A. Zielińska, E. Poleszak, J. Fichna, P. Wlaź, The role of microbiota-gut-brain axis in neuropsychiatric and neurological disorders, Pharmacol. Res. 172 (2021) 105840, https://doi.org/10.1016/j.phrs.2021.105840.

[19] L. Chang, Y. Wei, K. Hashimoto, Brain–gut–microbiota axis in depression: a historical overview and future directions, Brain Res. Bull. 182 (2022) 44–56, https://doi.org/10.1016/j.brainresbull.2022.02.004.

[20] A. Asadi, N. Shadab Mehr, M.H. Mohamadi, F. Shokri, M. Heidary, N. Sadeghifard, S. Khoshnood, Obesity and gut–microbiota–brain axis: a narrative review, Clin. Lab. Anal. 36 (2022), https://doi.org/10.1002/jcla.24420.

[21] W. Xiao, J. Su, X. Gao, H. Yang, R. Weng, W. Ni, Y. Gu, The microbiota-gut-brain axis participates in chronic cerebral hypoperfusion by disrupting the metabolism of short-chain fatty acids, Microbiome 10 (2022), https://doi.org/10.1186/s40168-022-01255-6.

[22] H. Ahmed, Q. Leyrolle, V. Koistinen, O. Kärkkäinen, S. Layé, N. Delzenne, K. Hanhineva, Microbiota-derived metabolites as drivers of gut–brain communication, Gut Microbes 14 (2022), https://doi.org/10.1080/19490976.2022.2102878.

[23] L.M.T. Dicks, Gut bacteria and neurotransmitters, Microorganisms 10 (2022) 1838, https://doi.org/10.3390/microorganisms10091838.

[24] D. Zhang, Y.-P. Jian, Y.-N. Zhang, Y. Li, L.-T. Gu, H.-H. Sun, M.-D. Liu, H.-L. Zhou, Y.-S. Wang, Z.-X. Xu, Short-chain fatty acids in diseases, Cell Commun. Signal. 21 (2023), https://doi.org/10.1186/s12964-023-01219-9.

[25] W. Pan, J. Zhao, J. Wu, D. Xu, X. Meng, P. Jiang, H. Shi, X. Ge, X. Yang, M. Hu, P. Zhang, R. Tang, N. Nagaratnam, K. Zheng, X.-F. Huang, Y. Yu, Dimethyl itaconate ameliorates cognitive impairment induced by a high-fat diet via the gut-brain axis in mice, Microbiome 11 (2023), https://doi.org/10.1186/s40168-023-01471-8.

[26] J. Beisner, L. Filipe Rosa, V. Kaden-Volynets, I. Stolzer, C. Günther, S.C. Bischoff, Prebiotic inulin and sodium butyrate attenuate obesity-induced intestinal barrier dysfunction by induction of antimicrobial peptides, Front. Immunol. 12 (2021), https://doi.org/10.3389/fimmu.2021.678360.

[27] X. Wang, Z. Wang, J. Cao, Y. Dong, Y. Chen, Gut microbiota-derived metabolites mediate the neuroprotective effect of melatonin in cognitive impairment induced by sleep deprivation, Microbiome 11 (2023), https://doi.org/10.1186/s40168-022-01452-3.

[28] X. Wang, C. Duan, Y. Li, H. Lu, K. Guo, X. Ge, T. Chen, Y. Shang, H. Liu, D. Zhang, Sodium butyrate reduces overnutrition-induced microglial activation and hypothalamic inflammation, Int. Immunopharmacol. 111 (2022) 109083, https://doi.org/10.1016/j.intimp.2022.109083.

[29] Z. Kovács, B. Brunner, C. Ari, Beneficial effects of exogenous ketogenic supplements on aging processes and age-related neurodegenerative diseases, Nutrients 13 (2021) 2197, https://doi.org/10.3390/nu13072197.

[30] A.P. Princivalle, GABAB receptors in neurodegeneration, Curr. Topics Behav. Neurosci. (2021) 267–290, https://doi.org/10.1007/7854_2021_222.

[31] A. Sood, K. Preeti, V. Fernandes, D.K. Khatri, S.B. Singh, Glia: a major player in glutamate–GABA dysregulation-mediated neurodegeneration, J. Neurosci. Res. 99 (2021) 3148–3189, https://doi.org/10.1002/jnr.24977.

[32] K. Kaźmierczak-Siedlecka, L. Marano, E. Merola, F. Roviello, K. Połom, Sodium butyrate in both prevention and supportive treatment of colorectal cancer, Front. Cell. Infect. Microbiol. 12 (2022), https://doi.org/10.3389/fcimb.2022.1023806.

[33] X. Yan, Y. Feng, Y. Hao, R. Zhong, Y. Jiang, X. Tang, D. Lu, H. Fang, M. Agarwal, L. Chen, Y. Zhao, H. Zhang, Gut-testis Axis: microbiota prime metabolome to increase sperm quality in young type 2 diabetes, Microbiol. Spectr. 10 (2022), https://doi.org/10.1128/spectrum.01423-22.

[34] X. Zhu, K. Li, G. Liu, R. Wu, Y. Zhang, S. Wang, M. Xu, L. Lu, P. Li, Microbial metabolite butyrate promotes anti-PD-1 antitumor efficacy by modulating T cell receptor signaling of cytotoxic CD8 T cell, Gut Microbes 15 (2023), https://doi.org/10.1080/19490976.2023.2249143.

[35] M.H. Costa, D.T.S. Ferreira, J.E.S. Pádua, J.P.A. Fernandes, J.C.C. Santos, F.A. S. Cunha, M.C.U. Araujo, A fast, low-cost, sensitive, selective, and non-laborious method based on functionalized magnetic nanoparticles, magnetic solid-phase extraction, and fluorescent carbon dots for the fluorimetric determination of copper in wines without prior sample treatment, Food Chem. 363 (2021) 130248, https://doi.org/10.1016/j.foodchem.2021.130248.

[36] Z. Gong, H.T. Chan, Q. Chen, H. Chen, Application of nanotechnology in analysis and removal of heavy metals in food and water resources, Nanomaterials 11 (2021) 1792, https://doi.org/10.3390/nano11071792.

[37] V.O. Shipunova, O.A. Kolesnikova, P.A. Kotelnikova, V.D. Soloviev, A.A. Popov, G. M. Proshkina, M.P. Nikitin, S.M. Deyev, Comparative evaluation of engineered polypeptide scaffolds in HER2-targeting magnetic nanocarrier delivery, ACS Omega 6 (2021) 16000–16008, https://doi.org/10.1021/acsomega.1c01811.

[38] P. Feng, Y. Che, C. Gao, X. Chu, Z. Li, L. Li, J. Li, J. Gao, Y. Dong, Profibrotic role of transcription factor SP1 in cross-talk between fibroblasts and M2 macrophages, iScience 26 (2023) 108484, https://doi.org/10.1016/j.isci.2023.108484.

[39] S. Yang, J. Xiang, C. Ma, G. Yang, X. Wang, H. Liu, G. Fan, L. Kang, Z. Liang, Sp1-like protein KLF13 acts as a negative feedback regulator of TGF-β signaling and fibrosis, Cell Rep. 42 (2023) 112367, https://doi.org/10.1016/j.celrep.2023.112367.

[40] H. Zheng, H. Xue, C. Zhang, The oncogenic roles of JC polyomavirus in cancer, Front. Oncol. 12 (2022), https://doi.org/10.3389/fonc.2022.976577.

[41] Z. Pan, K. Wang, X. Wang, Z. Jia, Y. Yang, Y. Duan, L. Huang, Z.-X. Wu, J. Zhang, X. Ding, Cholesterol promotes EGFR-TKIs resistance in NSCLC by inducing EGFR/Src/Erk/SP1 signaling-mediated ERRα re-expression, Mol. Cancer 21 (2022), https://doi.org/10.1186/s12943-022-01547-3.

[42] A.K. Verma, A. Sharma, N. Subramaniyam, C.R. Gandhi, Augmenter of liver regeneration: mitochondrial function and steatohepatitis, J. Hepatol. 77 (2022) 1410–1421, https://doi.org/10.1016/j.jhep.2022.06.019.

[43] J. Song, S. Nabeel-Shah, S. Pu, H. Lee, U. Braunschweig, Z. Ni, N. Ahmed, E. Marcon, G. Zhong, D. Ray, K.C.H. Ha, X. Guo, Z. Zhang, T.R. Hughes, B. J. Blencowe, J.F. Greenblatt, Regulation of alternative polyadenylation by the C2H2-zinc-finger protein Sp1, Mol. Cell 82 (2022) 3135–3150.e9, https://doi.org/10.1016/j.molcel.2022.06.031.

[44] Y. Hui, Z. Xu, J. Li, L. Kuang, Y. Zhong, Y. Tang, J. Wei, H. Zhou, T. Zheng, Nonenzymatic function of DPP4 promotes diabetes-associated cognitive dysfunction through IGF-2R/PKA/SP1/ERp29/IP3R2 pathway-mediated impairment of Treg function and M1 microglia polarization, Metabolism 138 (2023) 155340, https://doi.org/10.1016/j.metabol.2022.155340.

[45] Q. Zhang, J. Zheng, W. Wu, H. Lian, N. Iranzad, E. Wang, L. Yang, X. Wang, X. Jiang, TRIM56 acts through the IQGAP1-CDC42 signaling axis to promote glioma cell migration and invasion, Cell Death Dis. 14 (2023), https://doi.org/10.1038/s41419-023-05702-6.

[46] T. Pang, Q. Tang, J. Wei, J. Li, L. Ma, Q. Qin, J. Ma, H. He, Y. Chen, Construction of a novel immune-related prognostic-predicting model of gastric cancer, Gene 852 (2023) 147032, https://doi.org/10.1016/j.gene.2022.147032.

[47] G. Chen, K. Tong, S. Li, Z. Huang, S. Liu, H. Zhu, Y. Zhong, Z. Zhou, G. Jiao, F. Wei, N. Chen, Extracellular vesicles released by transforming growth factor-beta 1-preconditional mesenchymal stem cells promote recovery in mice with spinal cord injury, Bioact. Mater. 35 (2024) 135–149, https://doi.org/10.1016/j.bioactmat.2024.01.013.
[48] C. Yang, P. Xu, The role of transforming growth factor β1/Smad pathway in Alzheimer's disease inflammation pathology, Mol. Biol. Rep. 50 (2022) 777–788, https://doi.org/10.1007/s11033-022-07951-8.
[49] M. Kapoor, S. Chinnathambi, TGF-β1 signalling in Alzheimer's pathology and cytoskeletal reorganization: a specialized Tau perspective, J. Neuroinflammation 20 (2023), https://doi.org/10.1186/s12974-023-02751-8.
[50] L. Zhang, T. Wang, D. Valle, Reduced PLP2 expression increases ER-stress-induced neuronal apoptosis and risk for adverse neurological outcomes after hypoxia ischemia injury, Hum. Mol. Genet. 24 (2015) 7221–7226, https://doi.org/10.1093/hmg/ddv422.
[51] L. Poupon-Bejuit, A. Geard, N. Millicheap, E. Rocha-Ferreira, H. Hagberg, C. Thornton, A.A. Rahim, Diabetes drugs activate neuroprotective pathways in models of neonatal hypoxic-ischemic encephalopathy, EMBO Mol. Med. 16 (2024) 1284–1309, https://doi.org/10.1038/s44321-024-00079-1.
[52] R. McCarthy, C. Martin-Fairey, D.K. Sojka, E.D. Herzog, E.S. Jungheim, M.J. Stout, J.C. Fay, M. Mahendroo, J. Reese, J.L. Herington, E.J. Plosa, E.L. Shelton, S. K. England, Mouse models of preterm birth: suggested assessment and reporting guidelines, Biol. Reprod. (2018), https://doi.org/10.1093/biolre/ioy109.
[53] H.D. Kanal, S.W. Levison, Neuroprotective effects of delayed TGF-β1 receptor antagonist administration on perinatal hypoxic-ischemic brain injury, Dev. Neurosci. 46 (2023) 188–200, https://doi.org/10.1159/000531650.
[54] Y. Sun, H. Wang, P. Wang, K. Zhang, X. Geng, Q. Liu, X. Wang, Tumor targeting DVDMS-nanoliposomes for an enhanced sonodynamic therapy of gliomas, Biomater. Sci. 7 (2019) 985–994, https://doi.org/10.1039/c8bm01187g.
[55] L. Bai, Y. Liu, K. Guo, K. Zhang, Q. Liu, P. Wang, X. Wang, Ultrasound facilitates naturally equipped exosomes derived from macrophages and blood serum for orthotopic glioma treatment, ACS Appl. Mater. Interfaces 11 (2019) 14576–14587, https://doi.org/10.1021/acsami.9b00893.
[56] B.P. Mead, N. Kim, G.W. Miller, D. Hodges, P. Mastorakos, A.L. Klibanov, J. W. Mandell, J. Hirsh, J.S. Suk, J. Hanes, R.J. Price, Novel focused ultrasound gene therapy approach noninvasively restores dopaminergic neuron function in a rat Parkinson's disease model, Nano Lett. 17 (2017) 3533–3542, https://doi.org/10.1021/acs.nanolett.7b00616.
[57] C.-Y. Wu, R.-Y. Huang, E.-C. Liao, Y.-C. Lin, Y.-J. Ho, C.-W. Chang, H.-L. Chan, Y.-Z. Huang, T.-H. Hsieh, C.-H. Fan, C.-K. Yeh, A preliminary study of Parkinson's gene therapy via sono-magnetic sensing gene vector for conquering extra/intracellular barriers in mice, Brain Stimul. 13 (2020) 786–799, https://doi.org/10.1016/j.brs.2020.02.024.
[58] J.S.D. Reis, A. Dos Reis Teixeira, A. De Vasconcelos Quaresma, T.C. Almeida, R. G. Arribada, J.T. Neto, F.H.R. Da Silva, A. Silva-Cunha, S.A. Lima De Moura, G. N. Da Silva, S.L. Fialho, G.R. Da Silva, Sodium butyrate-loaded nanoparticles coated with chitosan for the treatment of neovascularization in age-related macular degeneration: ocular biocompatibility and antiangiogenic activity, Eur. J. Pharm. Biopharm. 179 (2022) 26–36, https://doi.org/10.1016/j.ejpb.2022.08.011.
[59] C.M. Melo, J.F. Cardoso, F.B. Perassoli, A.S. de Oliveira Neto, L.M. Pinto, M.B. de Freitas Marques, W. da Nova Mussel, J.T. Magalhães, S.A. de Lima Moura, M.G. de Freitas Araújo, G.R. Da Silva, Amphotericin B-loaded Eudragit RL100 nanoparticles coated with hyaluronic acid for the treatment of vulvovaginal candidiasis, Carbohydr. Polym. 230 (2020) 115608, https://doi.org/10.1016/j.carbpol.2019.115608.
[60] J.F. Cardoso, F.B. Perasoli, T.C. Almeida, M.B.D.F. Marques, C.R. Toledo, P.O. Gil, H.D.S. Tavares, M.C. Da Paz, W.D.N. Mussel, J.T. Magalhães, G.N.D. Silva, A. Da Silva-Cunha, P.A. Granjeiro, A.M. Klibanov, G.R. Da Silva, Vancomycin-loaded N, N-dodecyl,methyl-polyethylenimine nanoparticles coated with hyaluronic acid to treat bacterial endophthalmitis: development, characterization, and ocular biocompatibility, Int. J. Biol. Macromol. 169 (2021) 330–341, https://doi.org/10.1016/j.ijbiomac.2020.12.057.
[61] J. Matowicka-Karna, Markery zapalenia, aktywacja płytek krwi i zaburzenia krzepnięcia w chorobach zapalnych jelit, Postepy Hig. Med. Dosw. 70 (2016) 305–312, https://doi.org/10.5604/17322693.1199305.
[62] S. Ristovska, O. Stomnaroska, D. Danilovski, Hypoxic ischemic encephalopathy (HIE) in term and preterm infants, Prilozi 43 (2022) 77–84, https://doi.org/10.2478/prilozi-2022-0013.
[63] M.C. Starr, J.R. Charlton, R. Guillet, K. Reidy, T.E. Tipple, J.G. Jetton, A.L. Kent, C. L. Abitbol, N. Ambalavanan, M.J. Mhanna, D.J. Askenazi, D.T. Selewski, M. W. Harer, Advances in neonatal acute kidney injury, Pediatrics 148 (2021), https://doi.org/10.1542/peds.2021-051220.
[64] N. Reddy, M. Doyle, P. Hanagandi, A. Taranath, H. Dahmoush, P. Krishnan, O. Oztekin, E. Boltshauser, M. Shroff, K. Mankad, Neuroradiological mimics of periventricular leukomalacia, J. Child Neurol. 37 (2021) 151–167, https://doi.org/10.1177/08830738211026052.
[65] N.N. Zavadenko, V.I. Guzeva, D.D. Gaynetdinova, L.A. Davydova, A.N. Zavadenko, T.A. Romanova, Pharmacotherapy of psychomotor developmental delay in 6-12 months preterm infants with hypoxic-ischemic encephalopathy (the double-blind comparative multicenter placebo-controlled study), Z. Nevrol. Psikhiatr. Im. S.S. Korsakova 119 (2019) 30, https://doi.org/10.17116/jnevro201911910130.
[66] H. Zhou, D.S. Chen, C.J. Hu, X. Hong, J. Shi, Y. Xiao, Stimuli-responsive nanotechnology for RNA delivery, Adv. Sci. 10 (2023), https://doi.org/10.1002/advs.202303597.
[67] Q. Hu, Z. Fang, J. Ge, H. Li, Nanotechnology for cardiovascular diseases, Innovation 3 (2022) 100214, https://doi.org/10.1016/j.xinn.2022.100214.
[68] B. Li, J. Mao, J. Wu, K. Mao, Y. Jia, F. Chen, J. Liu, Nano–bio interactions: biofilm-targeted antibacterial nanomaterials, Small 20 (2023), https://doi.org/10.1002/smll.202306135.
[69] S. Bhattacharya, A. Agrawal, Cutting-edge nanotechnological approaches for lung cancer therapy, CDRR 14 (2022) 171–187, https://doi.org/10.2174/2589977514666220418085658.
[70] A. Sharma, D. Shambhwani, S. Pandey, J. Singh, H. Lalhlenmawia, M. Kumarasamy, S.K. Singh, D.K. Chellappan, G. Gupta, P. Prasher, K. Dua, D. Kumar, Advances in lung cancer treatment using nanomedicines, ACS Omega 8 (2022) 10–41, https://doi.org/10.1021/acsomega.2c04078.
[71] L. Liu, M. Sadaghian Sadabad, G. Gabarrini, P. Lisotto, J.Z.H. von Martels, H. R. Wardill, G. Dijkstra, R.E. Steinert, H.J.M. Harmsen, Riboflavin supplementation promotes butyrate production in the absence of gross compositional changes in the gut microbiota, Antioxidants Redox Signal. (2022), https://doi.org/10.1089/ars.2022.0033.
[72] J.H. Cho, C.W. Chae, J.R. Lim, Y.H. Jung, S.J. Han, J.H. Yoon, J.Y. Park, H.J. Han, Sodium butyrate ameliorates high glucose-suppressed neuronal mitophagy by restoring PRKN expression via inhibiting the RELA-HDAC8 complex, Autophagy 20 (2024) 1505–1522, https://doi.org/10.1080/15548627.2024.2323785.
[73] Y. Xu, S. Wei, L. Zhu, C. Huang, T. Yang, S. Wang, Y. Zhang, Y. Duan, X. Li, Z. Wang, W. Pan, Low expression of the intestinal metabolite butyric acid and the corresponding memory pattern regulate HDAC4 to promote apoptosis in rat hippocampal neurons, Ecotoxicol. Environ. Saf. 253 (2023) 114660, https://doi.org/10.1016/j.ecoenv.2023.114660.
[74] M.A.F. Caetano, H.I.R. Magalhães, J.R.L. Duarte, L.B. Conceição, P. Castelucci, Butyrate protects myenteric neurons loss in mice following experimental ulcerative colitis, Cells 12 (2023) 1672, https://doi.org/10.3390/cells12131672.
[75] P. Xiao, X. Cai, Z. Zhang, K. Guo, Y. Ke, Z. Hu, Z. Song, Y. Zhao, L. Yao, M. Shen, J. Li, Y. Huang, L. Ye, L. Huang, Y. Zhang, R. Liu, M. Xu, X. Xu, Y. Zhao, Q. Cao, Butyrate prevents the pathogenic anemia-inflammation circuit by facilitating macrophage iron export, Adv. Sci. 11 (2024), https://doi.org/10.1002/advs.202306571.
[76] M. Snelson, C. de Pasquale, E.I. Ekinci, M.T. Coughlan, Gut microbiome, prebiotics, intestinal permeability and diabetes complications, Best Pract. Res. Clin. Endocrinol. Metabol. 35 (2021) 101507, https://doi.org/10.1016/j.beem.2021.101507.
[77] X. Xu, X. Wang, L. Zhang, Y. Jin, L. Li, M. Jin, L. Li, H. Ni, Nicotinamide adenine dinucleotide treatment confers resistance to neonatal ischemia and hypoxia: effects on neurobehavioral phenotypes, Neural Regen. Res. 19 (2024) 2760–2772, https://doi.org/10.4103/nrr.nrr-d-23-01490.
[78] K. Zhu, X. Zhu, S. Sun, W. Yang, S. Liu, Z. Tang, R. Zhang, J. Li, T. Shen, M. Hei, Inhibition of TLR4 prevents hippocampal hypoxic-ischemic injury by regulating ferroptosis in neonatal rats, Exp. Neurol. 345 (2021) 113828, https://doi.org/10.1016/j.expneurol.2021.113828.
[79] Y. Yang, Y. Li, W. Yang, X. Yang, M. Luo, L. Qin, J. Zhu, Protecting effects of 4-octyl itaconate on neonatal hypoxic-ischemic encephalopathy via Nrf2 pathway in astrocytes, J. Neuroinflammation 21 (2024), https://doi.org/10.1186/s12974-024-03121-8.
[80] M. Zjalić, M. Mustapić, Z. Glumac, I. Prološčić, S. Blažetić, A. Vuković, M. Masud, M. Billah, A. Khan, S. Šegota, M.S.A. Hossain, M. Heffer, Construction of AC/DC magnetic syringe device for stimulated drug release, injection and ejection of nanocarriers and testing cytotoxicity in vitro, MethodsX 8 (2021) 101312, https://doi.org/10.1016/j.mex.2021.101312.
[81] T. Pineda-Vásquez, L. Rendón-Castrillón, M. Ramírez-Carmona, C. Ocampo-López, From E-waste to high-value materials: sustainable synthesis of metal, metal Oxide, and MOF nanoparticles from waste printed circuit boards, Nanomaterials 14 (2023) 69, https://doi.org/10.3390/nano14010069.
[82] E. Okulu, I.M. Hirfanoglu, M. Satar, O. Erdeve, E. Koc, F. Ozlu, An observational, multicenter, registry-based cohort study of Turkish Neonatal Society in neonates with Hypoxic ischemic encephalopathy, PLoS One 18 (2023) e0295759, https://doi.org/10.1371/journal.pone.0295759.